

ELECTROMAGNETS FOR HIGH-ENERGY PHYSICS APPLICATIONS

H. Brechna

Stanford Linear Accelerator Center
Stanford University, Stanford, California

Abstract

The multi-functional purpose of powerful electromagnets to be used for high-energy physics applications requires specific features such as magnetic field strength, field homogeneity in a requested space, field configuration and distribution, resolution, solid angle, dispersion and focusing properties. These demands are easily met if boundary conditions such as dimensional and material limitations, geometrical and environmental effects, power consumption, and adequate cooling are not restricted.

The paper deals with magnets which fulfill as closely as possible the above requirements, considering actual limitations given by conditions in laboratories as well as dimensional, geometrical, and material properties.

An approach to designing iron-bound magnets using Fabry factors is given. Coil configuration, pole form and shaping, iron boundaries; impurities in ferromagnetic materials, cooling methods and media, and magnet performance are explored. Magnet design features such as reliability, choice of conductor, magnetic materials, and coil insulation are included. Coil damage due to fatigue, electrical breakdown, moisture and other influences on insulation, and environmental conditions are discussed.

I. Introduction

In recent years, the electromagnet has grown to become one of the most important (as well as one of the most expensive) parts of high-energy accelerators - so much so, in fact, that in modern physics we can not envision any high-energy accelerator without the use of electromagnets. They are used for many purposes in different areas, such as steering, bending, focusing, separating particles, and momentum analysis, as beam transport devices, and in experimental areas such as in spectrometers, spark chambers, and bubble chambers.

In circular accelerators, the magnet function frequently is to bend particles to keep them in orbit and to provide framing force, to restrict their horizontal and vertical motion, so that the particles remain well inside the vacuum tubings and chambers.

In linear accelerators the two functions can be separated. The provision of focusing forces is done by the use of magnetic focusing lenses, and the steering and bending are provided by constant-gradient magnets.

The magnet in a high-energy system is not an independent entity. Its design is influenced by other components such as the vacuum system, the injector control system, and the buildings.

The requirements for magnetic fields, their shape; homogeneity; and optical properties have increased considerably with the growth of accelerators. In early stages of magnet design, simple

calculations based on known engineering practices and, in a few cases, scaled models were sufficient to satisfy most requirements. For modern accelerators a vast team effort combining scaled models, conducting developmental work, study of materials and insulation, computer calculations, and the use of precise and sophisticated field and mechanical tolerance measuring techniques and devices are necessary before the optimally designed magnet is realized.

The function of the magnet design group is also manifold. It must maintain close contact with component design groups as well as the theoretical or experimental physicist in order to know the future role, purpose, and extensions of the magnet to be designed. It must bear in mind the capabilities of the manufacturer, who will provide the components and parts of the magnet. Unfortunately, it is not always possible to use standard parts and straight manufacturing techniques due to the predominant requirements of the accelerator; i.e., the use of special thermosets may be necessary to protect the insulation from radiation damage, and complicated pole shaping may have to be done to provide high homogeneity fields in gaps or a certain field gradient in AGS magnets. However, radical departures from standard manufacturing techniques often lead to undesirable delays and frustration due to lengthening of delivery schedule.

The magnet design group has to plan the magnet delivery program to fit the overall accelerator program, and therefore provide ample time for research, design and magnet procurement.

It is not the purpose of this report to cover all possible and basic problems for various types of magnets. However, basic requirements are common among the majority of magnet types; these will be dealt with below.

II. Optical Definitions

Electromagnets may be divided basically into a few main groups: alternating-field ac and dc magnets and constant-field ac and dc magnets. In both cases, the magnetic field within a useful volume over a certain time period must follow a pre-chosen pattern. Any dc magnet may be considered as a special case of alternating field magnets; therefore, the theoretical studies on field shaping remain the same in both cases.

A number of common requirements on all high-energy magnets are discussed by several authors^{1,2} but are scattered in various reports, so that a brief summary at this point seems appropriate.

A. Symmetry Planes

We confine our discussion to magnets having a symmetry plane. In Cartesian coordinates, the potential function can be written as scalar

$$V(x, y, z) = -V(x, -y, z) \quad (1)$$

B. Field Homogeneity

Field homogeneity is normally defined over the symmetry plane. However, in a more generalized form it should be noted as

$$\epsilon = 1 - \frac{\vec{B}(x,y,z)}{\vec{B}(0,0,0)} \quad (2)$$

where $\vec{B}(0,0,0)$ denotes the field vector in the gap or bore center. Equation (2) may also be adapted as the definition of field-gradient at any point in space.

C. Phase Space

The beam of monoenergetic particles with no appreciable coupling between horizontal and vertical motions can be described by means of density distribution in the horizontal and vertical phase planes. All particles of interest are contained within an area bounded by a closed curve in each phase plane.

With "s" being the coordinate along the beam axis and $x(s)$, $x'(s) = dx/ds = \theta$; the transverse deviations and the angular divergence of the particles may be written for all closed curves in a normalized form (see Fig. 1a):

$$Cx^2 + 2Dxx' + Fx'^2 = E \quad (3)$$

and

$$A = CF - D^2 \quad (4)$$

as the determinate of Eq. (3).

We define

$F^{1/2}$ = Displacement profile

$C^{1/2}$ = Divergence profile

$E = (\Lambda^{1/2}/\pi) \cdot A$ = emittance, with A as the area of the ellipse.

D determines the orientation of the phase ellipse in phase space.

The range of variables $x_0, \theta_0, y_0, \phi_0$, and $\Delta p/p$ for the coordinates at a point P and the importance of one or several of them must be considered for specific cases. A unit set does not necessarily define all magnet types or combinations. For a monochromatic beam and a point source,

$$x_0 = y_0 = \frac{\Delta p}{p} \Big|_0 = 0$$

where the phase space is defined as:

$$\langle \theta_0, \phi_0 \rangle = \Omega \quad (5)$$

and Ω is defined as solid angle.

For particles with momentum p_x at x , the phase ellipse is defined as (see Fig. 1b)

$$Cx^2 + 2Dxp + Fp^2 = E$$

with

$$x_m^2 = \frac{F}{CF - B^2}$$

and the admittance

$$A = \int dp_x \cdot dx$$

For a periodic system of focusing elements, the transfer matrix for first-order optics is written³

$$\begin{pmatrix} x_n \\ p_n \end{pmatrix} = \begin{pmatrix} a_{11} & a_{12} \\ a_{21} & a_{22} \end{pmatrix}^n \begin{pmatrix} x_{n-1} \\ p_{n-1} \end{pmatrix} \\ = \begin{pmatrix} A_{11}(n) & A_{12}(n) \\ A_{21}(n) & A_{22}(n) \end{pmatrix} \begin{pmatrix} x_{n-1} \\ p_{n-1} \end{pmatrix}$$

where

$$A_{11}(n) = \cos(n\theta) + \frac{a_{11} - a_{22}}{2} \cdot \frac{\sin(n\theta)}{\sin\theta}$$

$$A_{12}(n) = a_{12} \cdot \frac{\sin(n\theta)}{\sin\theta}$$

$$A_{21}(n) = a_{21} \cdot \frac{\sin(n\theta)}{\sin\theta}$$

$$A_{22}(n) = \cos(n\theta) - \frac{a_{11} - a_{22}}{2} \cdot \frac{\sin(n\theta)}{\sin\theta}$$

and

$$\cos\theta = \frac{1}{2}(a_{11} - a_{12})$$

The acceptance region of particles is an elliptical cone with the semi-major angle α and semi-minor angle β . The solid angle is given by

$$\Omega = \pi\alpha\beta$$

D. Resolution

If the displacement at the image point is x_1 , the beam resolution with the x_0, y_0 source coordinate is defined in first order as

$$R_{1st\ order} = -\frac{D}{M} \frac{1}{x_0} \quad (6)$$

where M is the magnification $x_1: x_0$ and D the momentum dispersion. For second-order resolution,

$$R_{2\text{nd order}} = \frac{D}{x_1} \quad (7)$$

where

$$x_1 = \langle x | x_0^2 \rangle \cdot x_0^2 + \langle x | \varphi_0^2 \rangle \cdot \varphi_0^2 + \langle x | x_0 \varphi_0 \rangle \cdot x_0 \varphi_0$$

E. General Field Equations for Magnets with Median Planes*

The existence of median planes requires that the potential V be an odd function; i.e.,

$$V(x, y, s) = V(x, -y, s)$$

In terms of a series expansion (Fig. 2),

$$V(x, y, s) = \sum_{\mu=0}^{\infty} \sum_{\nu=0}^{\infty} \frac{C(s)}{(2\mu+1, \nu)} \cdot \frac{x^\nu}{\nu!} \cdot \frac{y^{2\mu+1}}{(2\mu+1)!} \quad (8)$$

and the fields are:

$$B_x = \frac{\partial V}{\partial x} = \sum_{\mu=0}^{\infty} \sum_{\nu=0}^{\infty} \frac{C(s)}{(2\mu+1, \nu+1)} \cdot \frac{x^\nu}{\nu!} \cdot \frac{y^{2\mu+1}}{(2\mu+1)!} \quad (9)$$

$$B_y = \frac{\partial V}{\partial y} = \sum_{\mu=0}^{\infty} \sum_{\nu=0}^{\infty} \frac{C(s)}{(2\mu+1, \nu)} \cdot \frac{x^\nu}{\nu!} \cdot \frac{y^{2\mu}}{(2\mu)!} \quad (10)$$

$$B_s = \frac{\rho}{\rho+x} \cdot \frac{\partial V}{\partial s} = \frac{\rho}{\rho+x} \cdot \sum_{\mu=0}^{\infty} \sum_{\nu=0}^{\infty} \frac{C'(s)}{(2\mu+1, \nu)} \cdot \frac{x^\nu}{\nu!} \cdot \frac{y^{2\mu+1}}{(2\mu+1)!} \quad (11)$$

with ρ as the bending radius of particles.
At the median plane for $y = 0$,

$$B_y = \sum_{\mu=0}^{\infty} \sum_{\nu=0}^{\infty} \frac{C(s)}{(2\mu+1, \nu)} \cdot \frac{x^\nu}{\nu!} \quad (12)$$

*The field equations in this chapter were first developed by Dr. K. Brown.

$$B_y = B_y \Big|_{x=0, y=0} + x \frac{\partial B_y}{\partial x} \Big|_{x=0, y=0} + \frac{x^2}{2!} \frac{\partial^2 B_y}{\partial x^2} \Big|_{x=0, y=0} + \dots \quad (13)$$

This corresponds to

$$C_{1\nu} = \frac{\partial^\nu B_y}{\partial x^\nu} \Big|_{x=0, y=0} \quad \text{functions of } s \text{ only.}$$

or in well-known form

$$B_y = B_{0,0,s} \left[1 - \frac{n(s)}{R(s)} \cdot x + \frac{m(s)}{R^2(s)} \cdot x^2 - \dots \right] \quad (14)$$

with

$$n = - \frac{R(s)}{B_y} \cdot \left(\frac{\partial B_y}{\partial x} \right) \Big|_{x=0, y=0}$$

$$m = \frac{R^2(s)}{2! B_y} \cdot \left(\frac{\partial^2 B_y}{\partial x^2} \right) \Big|_{x=0, y=0}$$

These equations generally may be modified for any special type of magnet.

The magnetic field in the y-s direction follows Eq. (15) (we assume magnets with magnetic mirrors) for symmetric cases; only even numbers of ν are encountered.

$$B_y = B_{0,0,s} \left[1 + \frac{R^2(s)}{2 \cdot B_y} \cdot \left(\frac{\partial^2 B_y}{\partial x^2} \right) \Big|_{x=0, y=0} x^2 + \dots \right] \quad (15)$$

For a given beam size and particle momentum the particle bending radius is a function of the magnet strength, defined as

$$\int B dl_{\text{eff}} = \frac{E}{c} \cdot b \quad (16)$$

with $\frac{E}{c} = p$ the particle momentum and b the bending angle in radians. The appropriate split between the choice of the maximum field B over

the median plane and the effective magnetic length l_{eff} is dictated by a number of requirements. A design with high flux density but short magnets gives high saturation in pole corners and the magnetic field homogeneity is jeopardized. To improve homogeneity inside a given gap volume, several methods are undertaken. One can increase the pole dimension, which leads to large magnets, or use pole shaping, and avoid excessive high flux density in corners. Auxiliary poles, pole-face windings, or the introduction of additional correcting magnets such as quadrupoles, sextupoles, and octupoles, are common practice. On the other hand, the increase in B requires high power consumption. Any magnet with low flux density in the gap will require more space and will be heavy and, for tight tolerances, more difficult to manufacture. However, such magnets may use less power. The right choice between maximum flux density, power consumption, the magnet size, and initial capital cost for each individual magnet type with respect to space and other components and parts, is important.

III. Field Homogeneity and Pole Shaping

The pole shape and cross-sectional area of the magnets are determined through studies of the dynamic motion of particles and from the first- and higher-order optical requirements. Basically the aperture inside the vacuum chamber must be large enough to accommodate the oscillation arising from the spread in space, angle, and energy of the beam. Due to the physical size of the beam, space in the x, y directions is needed for the particle excursion and phase oscillation, or mis-steering.

The cross-sectional size and pole shape of the magnet is mainly determined through studies of the dynamic motion of charged particles. The gap width is given by the size of vacuum chamber or experimental equipment located between the pole tips. The aperture inside the vacuum chamber must be sufficiently large to accommodate oscillations arriving from the beam spread in space. Radial space is needed for the excursion of the phase oscillation. The proper match of the pole size and contour to a required field shape over an aperture dictated by the trajectory equations is the main task in magnet design. The matching of the pole and, subsequently, gap dimensions to the vacuum tubes, etc., sets the magnet parameters and the requirements in buildings, power, cost of materials, etc. Most of the high-energy magnets are iron-core or iron-bound magnets, and the magnet outer dimensions as well as the power requirements are related to the desired field shape in the bore and the iron saturation.

For a chosen pole width, the magnet designer wants to achieve the maximum possible range of field homogeneity and constance of magnet strength $\int B dl$. This is possible by shaping the pole ends and the pole sides.

In this section we treat constant field magnets for rectangular-shaped poles, where circular symmetric poles may be considered as a special case of this three-dimensional problem and alternating gradient magnets (AGS) to be used in circular accelerators.

A. Field Profile in the x - y Plane Perpendicular to the Beam Direction

We assume that the pole contour at the beam entrance and exit does not affect the field in the y - x plane, which is true if $l_{\text{eff}} > 2w$. Rectangular poles with faces perpendicular to the pole surface are treated, as shown in Fig. 3.

For manufactured and tested magnets, the field profile over the midplane measured for the specific case of $h/g = 6$ and $w/g = 4$ gave the relative values of $B(x, 0, 0)/B(0, 0, 0) = f(x/g)$, which are plotted in Fig. 3. The curve follows the equation*

$$\frac{B(x, 0, 0)}{B(0, 0, 0)} = \frac{1}{1 + e^x} \quad (17)$$

with

$$X = c_0 + c_1 x + c_2 x^2 + c_3 x^3$$

and the constants computed as

$$c_0 = -1.373; c_1 = 4.25; c_2 = -2.1; c_3 = 0.52$$

For the case of iron permeability $\mu_r \gg 1$, the field calculations can be based on conformal mapping.^{5,6}

The field profile along the symmetry plane follows the equation

$$\frac{B(x, 0, 0)}{B(0, 0, 0)} = \text{real} \left(\frac{t - (g/h)^2}{t + 1} \right)^{1/2} \quad (18)$$

where the relation (z, t) can be taken from

$$z = x + jy = \frac{g}{\pi} \cdot \ell_n \left[\frac{1 + \frac{1}{t}}{1 - \frac{(g/h)^2}{t}} + 1 \right] - \frac{2i}{\pi} \tan^{-1} \left(\frac{t + 1}{\frac{t}{(g/h)^2} - 1} \right)^{1/2} \quad (19)$$

For $t \gg 1$, Eq. (18) is simplified to

$$\frac{B(x, 0, 0)}{B(0, 0, 0)} = \left[1 - \sum_{v=1}^{\infty} (-1)^v \cdot 2^{v+1} \cdot e^{-v(\frac{\pi x}{g} + 2)} \right]^{1/2} \quad (20)$$

A comparison between curves 1 and 2 in Fig. 3 reveals a divergence in the field profile although $B(0, y)$ is infinity in the mathematical treatment. Due to iron saturation, this does not represent actual fact. As a first approximation, however, a field calculation according to Eq. (18) is appropriate.

For many applications a field homogeneity $1-\epsilon = 10^{-4}$ in the midplane over $x/g > \pm (2 \dots 3)$ is desirable. In the above calculation we achieve $\epsilon = 0.99$ at $x/g = 1.9$ and $\epsilon = 0.8$ at $x/g = 0$. To correct this deficiency for a given pole width, or to reduce the pole width for a required field homogeneity, the poles must be skinned. Possible solutions^{5,6} to limit flux density in the pole sides in the x-y planes require that iron should be added to some parts of the pole and removed in other parts of a rectangular pole edge. The solution proposed by Hedin⁵ requires a graphical integration:

$$\int t(x) e^{\pi x/g} dx = 0.086 g^2 \quad (21)$$

with t the shim thickness.

The mathematical model used by Brechna⁶ uses curved boundaries. In Fig. 4 the corner model and the modification to arcs of circles are illustrated. The modified Schwarz-Christoffel equation for curved corners is

$$z = x+jy = \frac{g}{\pi} \lambda_2 \int \frac{(t+a)^{1/2} dt}{\left[(1-\lambda_1) + \lambda_1 \left(\frac{t+1}{t+a} \right)^{1/2} \right] t(t-c)^{1/2}} + \frac{g(1-\lambda_2)}{\pi} \int \frac{(t+b)^{1/2} dt}{\left[(1-\lambda_1) + \lambda_1 \left(\frac{t+1}{t+a} \right)^{1/2} \right] + (t-1)^{1/2}} + C \quad (22)$$

The potential difference between the pole and the midplane requires the form:

$$\frac{dW}{dz} = B_x + jB_y = \frac{V_0}{g} \left[\frac{\lambda_1 \left(\frac{t+1}{t+a} \right)^{1/2} + (1-\lambda_1)}{\lambda_2 + (1-\lambda_1) \left(\frac{t+b}{t+a} \right)^{1/2}} \right] \frac{(t-c)^{1/2}}{(t+a)^{1/2}} \quad (23)$$

The shape of the rounded corners is fixed by the choice of the constants λ_1 and λ_2 . To calculate the parameters $a \dots c$ for a given magnet, the following boundary values must be specified:

$$K_1 = g/h \quad K_2 = g_0/g \quad K_3 = \frac{B(t=-1)}{B(t=\infty)}$$

$$K_4 = \frac{B(t=-a)}{B(t=\infty)} \quad K_5 = j \cdot \frac{B(t=-b)}{B(t=-a)}$$

Equations (21) and (22) may be extended if desired over many more parameters. The simple case of one rounded corner is calculated below.

The Schwarz-Christoffel transformation for the pole contour as in Fig. 5 may be written:

$$z = \frac{g}{\pi} \int \frac{\lambda(t+1)^{1/2} + (1-\lambda)(t+a)^{1/2}}{t(t-b)^{1/2}} dt + C \quad (24)$$

The potential difference is

$$\frac{dW}{dz} = \frac{V_0}{g} \cdot \frac{(t-b)^{1/2}}{\lambda(t+1)^{1/2} + (1-\lambda)(t+a)^{1/2}} \quad (25)$$

with

$$b < a < 1.$$

For the pole contour $-1 < t < -a$, the equations of the pole contour can be expressed as

$$y = g \left[1 - \frac{2\lambda}{\pi} \tan^{-1} \left(\frac{1+t}{b-t} \right)^{1/2} + \frac{\lambda}{\pi(b)^{1/2}} \cdot \ln \frac{1 + \left[\frac{b(1+t)}{b-t} \right]^{1/2}}{1 - \left[\frac{b(1+t)}{b-t} \right]^{1/2}} \right]$$

$$x = \frac{g}{\pi} (1-\lambda) \left\{ \ln \frac{1 + \left(\frac{t+a}{t-b} \right)^{1/2}}{1 - \left(\frac{t+a}{t-b} \right)^{1/2}} - 2 \left(\frac{a}{b} \right)^{1/2} \cdot \tan^{-1} \left[\frac{b}{a} \frac{t+a}{t-b} \right]^{1/2} - \ln \frac{1 + \left(\frac{1-a}{1+b} \right)^{1/2}}{1 - \left(\frac{1-a}{1+b} \right)^{1/2}} + 2 \left(\frac{a}{b} \right)^{1/2} \cdot \tan^{-1} \left[\frac{b}{a} \cdot \frac{1-a}{1+b} \right]^{1/2} \right\} \quad (26)$$

For a given magnet pole profile,

$$K_1 = \frac{g}{h} = \frac{1}{\delta}$$

$$K_2 = \frac{B(t=-1)}{B(t=\infty)}$$

$$K_3 = j \frac{B(t=-a)}{B(t=-1)}$$

The constants a , b and λ are calculated for different cases and the field distribution is plotted in Fig. 3.

The model calculation has the advantage that for a given distribution of B_y required for particle optical reasons [Eq. (14)]

$$B_y = B_{o,o,s} \left[1 - \frac{n(s)}{R(s)} \cdot x + \frac{m(s)}{R^2(s)} \cdot x^2 - + \dots \right]$$

In the median plane, using Eq. (23),

$$B_y = \frac{V_o}{g} \cdot \text{real} \frac{\left[\lambda_1 \left(\frac{t+1}{t+a} \right)^{\frac{1}{2}} + (1-\lambda_1) \right] (t-c)^{\frac{1}{2}}}{\left[\lambda_2 + (1-\lambda_2) \left(\frac{t+b}{t+a} \right)^{\frac{1}{2}} \right] (t+a)^{\frac{1}{2}}}$$

or Eq. (25)

$$B_y = \frac{V_o}{g} \cdot \text{real} \frac{(t-b)^{1/2}}{\lambda(t+1)^{1/2} + (1-\lambda)(t+a)^{1/2}}$$

we can compute a , b , c , and λ . Inserting these values in Eqs. (24) and (26) for z or x and y in the simplified model, we can determine the pole contour for two-dimensional cases. The pole contour then obtained may be approximated by a set of straight lines in order to simplify manufacturing problems.

Numerical methods for flux plotting have been developed for establishing field patterns and the pole contour. In these methods the potential function is obtained by numerical solution of the second-order equation, which describes it. Compounding magnetic fields with nonrectangular pole boundaries, we face a deficiency in using the vector potential in relaxation calculations because of the necessity that at the air-iron boundary the normal derivative of the vector-potential must be zero. The virtual points in this boundary condition are not true set points.

For two-dimensional boundaries, a modified potential function ψ is proposed by Livingston and Blewett.⁷

$$B_y = - \frac{\partial \psi}{\partial y} = - \frac{\partial A}{\partial x}$$

$$B_x + \int_0^y \mu_1 I dy = - \frac{\partial \psi}{\partial x}$$

ψ behaves like a scalar potential in non-current-bearing regions and is related to the total current enclosed at a given point in current-bearing regions.

The Laplacian of ψ is given by

$$\nabla^2 \psi = \frac{\partial}{\partial x} \int_0^y \mu_1 I dy$$

$\nabla^2 \psi$ is zero at current-free regions and throughout the coil.

B. Pole Profile for Alternating Gradient Fields

Generally the pole shaping for AGS magnets are performed by means of relaxation methods for two-dimensional cases.^{8,9} A treatment based on conformal transformation is reported by A. Hardt.¹⁰ The hyperbolic pole contours in the Z -plane are transformed in the t -plane, where they convert to straight lines (Fig. 6). The transformation from the t -plane to the potential plane W is

$$\frac{dW}{dt} = \frac{y_s}{\phi_s} \cdot \frac{(1+t/\gamma)(1+t/\alpha)}{t(1+t)^{2-\alpha/\gamma}} \quad (27)$$

with $\gamma < 1 < \alpha$, y_s in the pole contour ordinate corresponding to x_s , the center of the particle orbit in the midplane

$$x_s = \frac{\rho_s}{n}$$

Using the relation

$$\theta = (1+t)^{\frac{1}{6}} = (1+\rho c j \rho_s)^{\frac{1}{6}}$$

Hardt calculated the pole contour for $\frac{\omega}{\pi} = \frac{5}{6}$:

$$z^2 = \frac{2x_s y_s}{\phi_s} [A(\theta) - A(\theta \rightarrow 1)]$$

with

$$A(\theta) = \frac{6}{\alpha \gamma} \left(\frac{\theta^5}{5} - \frac{(\alpha-1)(1-\gamma)}{\theta} \right) + \ell_n \frac{\theta-1}{\theta+1} + e^{-j\frac{\pi}{3}} \cdot \ell_n \frac{\theta-e^{j\frac{\pi}{3}}}{\theta+d^{j\frac{\pi}{3}}} + e^{j\frac{\pi}{3}} \cdot \ell_n \frac{\theta-e^{-j\frac{\pi}{3}}}{\theta+e^{j\frac{\pi}{3}}}$$

The field equation at the pole contour is given by

$$\left| \frac{B(x_s, y_s, s)}{B(o, o, o)} \right|^2 = \frac{(1 + 2\rho \cdot \cos \phi_s + \rho^2)^{\frac{7}{6}}}{\left[1 + \frac{2\rho}{\gamma} \cdot \cos \phi_s + \left(\frac{\rho}{\gamma} \right)^2 \right] \left[1 + \frac{2\rho}{\alpha} \cos \phi_s + \left(\frac{\rho}{\alpha} \right)^2 \right]} \quad (28)$$

and at the midplane,

$$\frac{B(x, o, s)}{B(o, o, o)} = \frac{x}{x_s} \frac{(1+t)^{\frac{7}{6}}}{\left(1 + \frac{t}{\alpha} \right) \left(1 + \frac{t}{\gamma} \right)} \quad (29)$$

The aperture confining the beam of strong-focusing AGS magnets is smaller than that of constant-field magnets. This may have a more significant influence on particle oscillations about their equilibrium orbit. Also, the desire to carry out several experiments requires that sufficient space must be provided to move and share the beam to various targets.

The pole shape which produces a constant field gradient is hyperbolic, assuming the flux leakage, the side gaps providing space for the coils and the coils themselves do not affect the field shape, which is only a first and crude approximation.

However, most computations are still for two-dimensional or axial symmetric poles. Two-dimensional model studies with resistance paper,¹¹ with stainless steel plates and sheets,¹² and three-dimensional studies with electrolytic tanks, as well as actual reduced or full size magnets, are aimed to determine the final pole and core shape, the forces on coils, and in the case of ac magnets, the core losses and the heating of the pole edges and ends.

C. Field Profile for Iron Profiles with Finite Permeability

The calculated values in Sections A and B do not represent values of finite permeability. Saturation in pole corners represents a shortening of the iron path. As a first approximation we may consider that the line of maximum field in the pole corner penetrates uninterrupted in the iron. Connecting points of equal flux, we derive the flux density and the permeability in iron, using the magnetization curve. The direction of the field line can be corrected from permeability ratio, and from Simpson's relation we obtain the average flux densities as a function of penetration depths. Using iterative methods, we finally derive the final equipotential line corresponding to the effective pole contour, shown in Fig. 7.

The contour line may be approximated by the polygon

$$z = x + jy = \frac{g}{\pi} \int \frac{\Pi(t + t_1)^{\frac{\alpha_1}{\pi}}}{t \cdot (t-b)^{\frac{1}{2}}} dt + C_2 \quad (30)$$

The field distribution is calculated from

$$B_y + jB_x = \frac{V_0}{\pi} \cdot \frac{1}{t} \cdot \frac{dt}{dz} = \frac{V_0}{g} \cdot \frac{(t-b)^{\frac{1}{2}}}{\Pi(t+t_1)^{\frac{\alpha_1}{\pi}}} \quad (31)$$

The evaluation of finite permeability is also possible, using the model calculations discussed in Section B. The maximum field in the pole contour is obtained for any medium plane field distribution; accordingly, the pole may be shaped such that pole corner saturation is avoided.

D. Field Profile at Pole Entrance and Exit

The pole end effects are known to be disturbing. Due to iron saturation in corners, the effective length of the magnet is reduced, and the field index is changed due to variation of $\int F dl = f \left(\frac{x}{g} \right)$ and as a function of the flux density in the medium plane. In case of ac magnets, the alternating field gradient in the end parts causes field disturbance and heating of the pole iron. Pole end shaping has been performed by Argonne, DECY, and SLAC and a summary of these efforts is given briefly.

We consider magnets with magnetic guard plates or mirrors. If the two pole end faces are perpendicular to the pole top surface, the same field equations are valid, as dealt with in Section A, for the xy plane. If we use the notation for the median plane

$$b(s) = \frac{B(o, o, s)}{B(o, o, o)}$$

and assume that $b(s)$ at the guard plate is small, we may work with an equivalent fringing field length (Fig. 8a)

$$l_e = \int_{-a_1}^{+a_2} b(s) ds - a_1 \quad (32)$$

The effective length of the magnet is defined as

$$l_{\text{eff}} = \int_{-l_t}^{l_t} b(s) ds \quad (33)$$

The pole ends may be shaped in the same manner, as discussed in Section A; however, at the pole corners at the intersection of the xy and yz planes, the problem is three-dimensional and an accurate analytic expression cannot be given presently. At the y, z plane with x=0, we discuss cases reported in lit. cit.:

b_1 : The gap is opened according to the relation¹³

$$\frac{y}{g} = \cos h(s/g) \quad (34)$$

The field profile at the midplane is calculated to be

$$\frac{B(o, o, s)}{B(o, o, o)} = (1 + e^{-2\pi s/g})^{-1} \quad (35)$$

and at the pole surface

$$\frac{B(o, jE, s)}{B(o, o, o)} = (1 + e^{-\pi s/g})^{-\frac{1}{2}} \quad (36)$$

The flux density over the pole in the y, s plane is constant. Figure 8b shows the field plot and the pole contour at the median plane.

b : The magnet gap is formed according to the relation⁶

$$sy^2 = \frac{g^3}{2 \tan \alpha} \quad (37)$$

The angle α is computed such that field perturbation at the intersection between straight and tapered pole surfaces is kept to a minimum. The field equation at the midplane is calculated to be

$$\frac{B(0,0,s)}{B(0,0,l)} = \frac{s_2 - s}{s_2 + s_1} \quad (38)$$

$$\text{for } -s_1 < s < +s_2$$

In both cases, the end profile in the $x-y$ plane will be extended over the shaped pole end, as shown in Fig. 8c. Comparisons of the field distribution for different cases are given in Fig. 3.

The length of the tapered pole part including the region for the coil must be:

$$s_2 > \frac{g}{2 \tan \alpha} \quad (39)$$

The advantage of this solution is that the effective magnet length changes proportionally to the magnetization current.

E. Effect of Coils

In previous sections it was assumed that coils were located far from the gap, so that they do not influence the pole fringing field. Actually, the coils are located close to the gap and their effect on the field pattern is not negligible.

The coil influence for quadrupole lenses is treated by Blewett¹⁴ and Hardt.¹⁰ A simple method of handling field superposition will be given below for a quadrupole magnet.

Assuming the poles of the magnetic lens are formed such that they produce a pure quadrupole field in region A, the potential and flux equations can be written as

$$V = 2k_1 xy \quad (40)$$

$$U = k_1 (x^2 - y^2) \quad (41)$$

The coil produces a homogeneous field with the potential and flux functions in the region B:

$$V = k_2 y \quad (42)$$

$$U = k_2 x \quad (43)$$

If the homogeneous field extends to a point x_0 on the ordinate (Fig. 9), the superposition of the flux equation leads to

$$k_1 (x^2 - y^2) - k_2 (x - x_0) - k_1 x_0^2 = 0 \quad (44)$$

and the superposition of the potential functions to

$$2k_1 xy - k_2 y = J(x) \quad (45)$$

From Eq. (44)

$$y = f(x) = \left[x^2 - x_0^2 - \frac{k_2}{k_1} (x - x_0) \right]^{\frac{1}{2}} \quad (46)$$

or

$$y^2 + \left(x_0 - \frac{k_2}{2k_1} \right)^2 = \left(x - \frac{k_2}{2k_1} \right)^2 \quad (47)$$

At a point $P(x_1, y_1)$ on the pole surface common to the quadrupoles and the homogeneous field region, by using the relation

$$\alpha = 1 - \frac{k_2}{2k_1 x_0}$$

we get

$$x_0 = x_1 \frac{1-\alpha}{1-2\alpha} \pm \left[x_1^2 \left(\frac{1-\alpha}{1-2\alpha} \right)^2 - \frac{x_1^2 - y_1^2}{1-2\alpha} \right]^{\frac{1}{2}}$$

The space distribution of current density in the coils may be calculated from

$$j(x, y) = \frac{J(x, y)}{2k_1 x_1 y_1} = \frac{xy}{x_1 y_1} \left[1 - \frac{x_0}{x} (1 - \alpha) \right] \quad (48)$$

The choice of x_0 is a matter of weighing the quadrupole field against the homogeneous field.

This method can be extended to superposition of quadrupole fields with different strength, quadrupole and sextupole fields, etc.

IV. Magnet Design

In large-volume experimental magnets, the iron functions not only as coil support, protection, and to shunt the stray field around the magnet in order that equipment may be placed close around the magnet, but it also contributes markedly to the field in the gap or bore produced by the coils.

A. Coils

In order to give a general idea on iron-bound large experimental magnets, we treat a case of a pair of Helmholtz coils confined by iron, as shown in Fig. 10.

For pairs of axial symmetric Helmholtz coils such as for bubble- and spark-chamber magnets, the axial field component from the coils alone with uniform current distribution may be calculated:^{15,16}

$$H_{zA} = \frac{1}{2} \mu_0 \lambda \iint \frac{S^2 \cdot y^2 dx dy}{[y^2 + (a-x)^2]^{\frac{3}{2}}} \quad (49)$$

for the case illustrated in Fig. 9 we integrate Eq. (49):

$$H_{zA} = \frac{1}{2} \mu_0 S \lambda a_1 \left\{ (\beta_1 - \gamma_1) \cdot \ln \left(\alpha \frac{1 + \left[1 + \left(\frac{\beta_1 - \gamma_1}{\alpha} \right)^2 \right]^{\frac{1}{2}}}{1 + \left[1 + (\beta_1 - \gamma_1)^2 \right]^{\frac{1}{2}}} \right) \right. \\ + (\beta_1 + \gamma_1) \ln \left(\alpha \frac{1 + \left[1 + \left(\frac{\beta_1 + \gamma_1}{\alpha} \right)^2 \right]^{\frac{1}{2}}}{1 + \left[1 + (\beta_1 + \gamma_1)^2 \right]^{\frac{1}{2}}} \right) \\ + (\beta_2 - \gamma_2) \cdot \ln \left(\alpha \frac{1 + \left[1 + \left(\frac{\beta_2 - \gamma_2}{\alpha} \right)^2 \right]^{\frac{1}{2}}}{1 + \left[1 + (\beta_2 - \gamma_2)^2 \right]^{\frac{1}{2}}} \right) \\ \left. + (\beta_2 + \gamma_2) \ln \alpha \frac{1 + \left[1 + \left(\frac{\beta_2 + \gamma_2}{\alpha} \right)^2 \right]^{\frac{1}{2}}}{1 + \left[1 + (\beta_2 + \gamma_2)^2 \right]^{\frac{1}{2}}} \right\} \quad (50)$$

$$H_{zA} = S \lambda a_1 \cdot F(\alpha; \beta_1; \beta_2; \gamma_1; \gamma_2) \frac{\mu_0}{2}$$

The relation between coil ampere-turns, current density S , and space factor λ is given by

$$S = \frac{IN_1}{2a_1^2 (\alpha-1) \lambda \beta_1} = \frac{IN_2}{2a_1^2 (\alpha-1) \lambda \beta_2} \\ = \frac{IN}{2a_1^2 (\alpha-1) \lambda (\beta_1 + \beta_2)} \quad (51)$$

for $\lambda_1 = \lambda_2 = \lambda$, and with the same radial dimensions for both coil sections, we get the power in

the coils

$$P = 2\pi S^2 \rho a_1^3 (\alpha^2 - 1) \lambda \left[\beta_1 + \beta_2 \right] \quad (52)$$

From Eqs. (50) and (52) we get the Fabry formula

$$H_{zA} = G \left(\frac{P \lambda}{a_1 \rho} \right)^{\frac{1}{2}} \quad (53)$$

with the geometry of Fabry factor

$$G = \frac{F}{\left[(\alpha^2 - 1) (\beta_1 + \beta_2) \right]^{\frac{1}{2}}} \cdot \frac{\mu_0}{(8\pi)^{\frac{1}{2}}} \quad (54)$$

The correct ratio $\beta_2/\beta_1 > 1$ must be found to achieve a certain field homogeneity to compensate for the field due to the iron shell. However, for each individual coil the well-known Fabry factors for constant current distribution can be used to check the optimum design of the magnet. Figure 11 gives a plot of G-factors for individual symmetric coils and uniform current density distribution as function of α and β . The field calculations in any point in space may be obtained from lit. cit.¹⁷

The case of rectangular Helmholtz pairs is treated by Grant;¹⁸ however, this work must be extended for unequal coil sections.

B. Core

The field contribution from iron core comes from aligned dipoles in the iron crystals. If the magnetic dipole m is oriented at an angle θ to the z axis, the field components in cylindrical coordinates are¹⁹ (Fig. 12):

$$B_z = \left[(3 \cos^2 \varphi - 1) \cdot \cos \theta \right. \\ \left. - 3 \cdot \sin \varphi \cdot \cos \varphi \cdot \sin \theta \right] \cdot \frac{m}{(x^3)} \cdot dv \quad (55)$$

$$B_r = \left[(3 \sin^2 \varphi - 1) \cdot \sin \theta \right. \\ \left. - 3 \cdot \sin \varphi \cos \varphi \cdot \cos \theta \right] \cdot \frac{m}{(x^3)} \cdot dv \quad (56)$$

Assuming uniform magnetization in iron, the field values are:

$$B_z = \int_{\psi_1}^{\psi_2} \left[(2z^2 - l^2) \cdot \cos \theta \right. \\ \left. - 3z l \cdot \sin \theta \right] \cdot \frac{Y \cdot A \cdot B \cdot M}{4\pi x^5} \cdot d\psi \quad (57)$$

Fig. 12

$$B_r = \int_{\psi_1}^{\psi_2} \left[(2l - z^2) \cdot \sin\theta - 3z^2 \cdot \cos\theta \right] \cdot \frac{Y \cdot AB \cdot M(Y \cdot \cos \psi - r)}{4\pi x^5 l} \cdot d\psi \quad (58)$$

The assumption of uniform field distribution in iron leads to errors of the order of 2% to 7%. For general iron shape, by using the field distribution in space from the coil geometry, applying the relation

$$\frac{\tan \gamma_1}{\tan \gamma_{1-}} = \frac{\mu_{r1}}{\mu_{r1-}}$$

and using Ampere's law for the $\oint H dl$, the magnetization curve for the iron used, the actual magnetization in iron can be calculated for three-dimensional iron geometry by successive approximation.

Another approach currently under investigation at SIAC is the solution of nonlinear quasi-Poisson equations. We start with Maxwell's equation

$$\nabla \times \left(\frac{1}{\mu} \nabla \times A \right) = S \quad (59)$$

or in expanded form

$$\frac{\partial}{\partial x} \left(\frac{1}{\mu} \frac{\partial A}{\partial x} \right) + \frac{\partial}{\partial y} \left(\frac{1}{\mu} \frac{\partial A}{\partial y} \right) + \frac{\partial}{\partial z} \left(\frac{1}{\mu} \frac{\partial A}{\partial z} \right) + S(x,y,z) = 0$$

where $A = A(x,y,z)$ is the vector potential and $\mu = \mu(x,y,z)$ the permeability. To calculate the field distribution in the core, magnetization curves and values of relative permeability obtained from various measurements at CERN and SIAC, shown in Fig. 13 and expressed in Eq. (60), are used to calculate Eq. (59).

For

$$0 < H \leq 700 \text{ At m}^{-1}$$

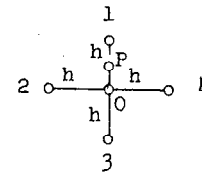
$$B = 16.91 \text{ H}$$

and

$$700 \leq H \leq 28 \times 10^3$$

$$B = \frac{17088}{e^{354}} + 43.1 (H)^{\frac{1}{2}} \quad (60)$$

The differential Eq. (59) is approximated by a difference equation by constructing a rectangular mesh with values of A and μ in the intersections. If the bar length between mesh points is h , we have at a point P:

$$\left. \frac{\partial A}{\partial x} \right|_P = \frac{A_1 - A_0}{h}$$


The diagram shows a central point 0 with four adjacent points: 1 above, 2 to the left, 3 below, and 4 to the right. The distance between any two adjacent points is labeled as 'h'.

$$\frac{1}{\mu} \left. \frac{\partial A}{\partial x} \right|_P = \frac{1}{2} \left(\frac{1}{\mu_1} + \frac{1}{\mu_0} \right) \left(\frac{A_1 - A_0}{h} \right)$$

and

$$\frac{\partial}{\partial x} \left(\frac{1}{\mu} \frac{\partial A}{\partial x} \right)_0 = \frac{1}{2h^2} \left[\left(\frac{1}{\mu_1} + \frac{1}{\mu_0} \right) (A_1 - A_0) + \left(\frac{1}{\mu_3} + \frac{1}{\mu_0} \right) (A_3 - A_0) \right]$$

$$\frac{\partial}{\partial y} \left(\frac{1}{\mu} \frac{\partial A}{\partial y} \right)_0 = \frac{1}{2h^2} \left[\left(\frac{1}{\mu_2} + \frac{1}{\mu_0} \right) (A_2 - A_0) + \left(\frac{1}{\mu_4} + \frac{1}{\mu_0} \right) (A_4 - A_0) \right]$$

In the two-dimensional case (x,y) we may write for Eq. (59)

$$A_0 \left[\sum_1^4 \left(\frac{1}{\mu_1} + \frac{1}{\mu_0} \right) \right] - \sum_1^4 \left(1 + \frac{1}{\mu_1} \right) A_i - 2h^2 S_0 = A_{\text{residual}}$$

As an example, the field distribution in the x,y plane of a bubble chamber with $2a=1.3$ meters is calculated with the computer B5500 and shown in Fig. 14. The SIAC computer program "Nutcracker" is being used for solutions of two-dimensional and axial symmetric cases.

The convergence of a mesh containing variable A and μ values is poor. If we consider one mesh as a system of finite difference equations, the convergence is achieved with the knowledge of the eigenvalues of the difference equation matrix. The eigenvalues depend on the geometry and boundary problem, and one may use Frankel's formula to approximate principal eigenvalues:

$$\omega = 2 - 2 \pi^{\frac{1}{2}} \left(\frac{1}{p^2} + \frac{1}{g^2} \right)^{\frac{1}{2}} \quad (61)$$

where ω is a convergence factor and p, g the numbers of nodes in the x,y direction.

The three-dimensional case can be solved by using the notation

$$\vec{A} = A_x(x,y,z) \hat{i} + A_y(x,y,z) \hat{j} + A_z(x,y,z) \hat{k}$$

$$\nabla \times \vec{H} = \nabla \times \left(\frac{1}{\mu} \nabla \times \vec{A} \right) = \vec{S}(x,y,z)$$

In terms of difference equations, the three components of $\nabla \times \vec{H}$ are written in the form

$$\frac{\partial}{\partial y} \left[\frac{1}{\mu} \frac{\partial A_y}{\partial x} - \frac{1}{\mu} \frac{\partial A_x}{\partial y} \right] - \frac{\partial}{\partial z} \left[\frac{1}{\mu} \frac{\partial A_x}{\partial z} - \frac{1}{\mu} \frac{\partial A_z}{\partial x} \right] = S_{x_0}(x, y, z)$$

$$\frac{\partial}{\partial z} \left[\frac{1}{\mu} \frac{\partial A_z}{\partial x} - \frac{1}{\mu} \frac{\partial A_x}{\partial z} \right] - \frac{\partial}{\partial x} \left[\frac{1}{\mu} \frac{\partial A_y}{\partial x} - \frac{1}{\mu} \frac{\partial A_x}{\partial y} \right] = S_{y_0}(x, y, z)$$

$$\frac{\partial}{\partial x} \left[\frac{1}{\mu} \frac{\partial A_x}{\partial z} - \frac{1}{\mu} \frac{\partial A_z}{\partial x} \right] - \frac{\partial}{\partial y} \left[\frac{1}{\mu} \frac{\partial A_z}{\partial y} - \frac{1}{\mu} \frac{\partial A_y}{\partial z} \right] = S_{z_0}(x, y, z)$$

The residual potential function can be written using the terminology in Fig. 15:

$$\begin{aligned} A_{x, \text{res}} = A_{x, 0} & \left[\frac{8}{\mu_0} + 2 \sum_{i=1}^4 \frac{1}{\mu_i} \right] + \frac{1}{\mu_1} (A'_{y_1} - A''_{y_1}) \\ & + \frac{1}{\mu_2} (A'_{z_2} - A''_{z_2}) - \frac{1}{\mu_3} (A'_{y_3} - A''_{y_3}) \\ & - \frac{1}{\mu_4} (A'_{z_4} - A''_{z_4}) - 4h^2 S_{x_0} \\ & - 2 \sum_{i=1}^4 \left(\frac{1}{\mu_0} + \frac{1}{\mu_i} \right) A_{x_i} \end{aligned}$$

$$\begin{aligned} A_{y, \text{res}} = A_{y, 0} & \left[\frac{8}{\mu_0} + 2 \sum_{i=1}^4 \frac{1}{\mu_i} \right] + \frac{1}{\mu_1} (A'_{z_1} - A''_{z_1}) \\ & + \frac{1}{\mu_2} (A'_{x_2} - A''_{x_2}) - \frac{1}{\mu_3} (A'_{z_3} - A''_{z_3}) \\ & - \frac{1}{\mu_4} (A'_{x_4} - A''_{x_4}) - 4h^2 S_{y_0} \\ & - 2 \sum_{i=1}^4 \left(\frac{1}{\mu_0} + \frac{1}{\mu_i} \right) A_{y_i} \end{aligned}$$

$$\begin{aligned} A_{z, \text{res}} = A_{z, 0} & \left[\frac{8}{\mu_0} + 2 \sum_{i=1}^4 \frac{1}{\mu_i} \right] + \frac{1}{\mu_1} (A'_{x_1} - A''_{x_1}) \\ & + \frac{1}{\mu_2} (A'_{y_2} - A''_{y_2}) - \frac{1}{\mu_3} (A'_{x_3} - A''_{x_3}) \\ & - \frac{1}{\mu_4} (A'_{y_4} - A''_{y_4}) - 4h^2 S_{z_0} \\ & - 2 \sum_{i=1}^4 \left(\frac{1}{\mu_0} + \frac{1}{\mu_i} \right) A_{z_i} \end{aligned}$$

V. Magnet Coils

The primary purpose of the coils is to provide enough ampere-turns to give the chosen magnetic field in the gap or working area. The splitting of the A_t in number of turns and current influences the size of the coil and, therefore, the magnet overall dimensions, the weight, and the power requirements.

Compact coils, with complicated two- and three-dimensional shape and high current density need better cooling provision, superior coil insulation, extensive and efficient cooling, and a thorough study of stresses due to temperature gradient, current, and magnetic forces. Coils with a large cross-sectional area and low current density lead to large overall coil dimensions and thus to expensive magnets. Due to limitations of manufacturers in producing long, hollow copper bars with large cross sections, one must solve the problems of joints, parallel cooling passage, and choice of material. In many cases, the coil must be adjusted to the power supply ratings, and in the case of large multi-megawatt magnets it is desirable that power supplies could be shared between different magnets. From extensive studies, it seems feasible to keep the applied voltage to the magnet terminals low, and design the magnet for a high current. The high power density in the coil requires direct cooling. To keep the temperature gradient in the coolant boundary layers down and to reduce frictional losses, the cooling media is in direct contact with the conductor. Present magnets with hollow conductors operate at a low water speed rate of 3-10 m/sec with Reynolds numbers > 2400 . The flow is turbulent. Higher water speeds, which may lead to copper erosion in case the water is in contact with air and for which protective measurements prove to be impractical, should be avoided. Studies carried out at CERN indicate that current densities of 600-1000 A cm^{-2} give the optimum magnet-power supply system. This number may very well vary between different high-energy laboratories in various countries.

In the design of magnet coils, the magnet designer faces the choice between different conductor materials, such as copper and copper alloys, aluminum and its alloys, the type of coolant, and cooling methods. In most magnets, high resistivity water is preferred over gases, insulating liquids, and cryogenic liquids for obvious reasons. Aluminum conductors can be obtained in very long lengths and are economically attractive, but most designers prefer copper to aluminum due to power consumption, even if the conductor length must be sacrificed. Continuous lengths of hollow copper conductors with cross sections up to $5 \times 5 \text{ cm}^2$ may be obtained in lengths up to 50 meters, and in smaller cross sections longer than 100 meters by a newly developed continuous casting process.

Regarding cooling methods, direct cooling is by far the most efficient. Square or rectangular conductor with circular or square holes is used extensively. With this type of cooling, a maximum heat flux of 4 watts/cm²/°C has been achieved by water passing through short lengths.¹⁶ In dc magnets with a hydraulic circuit of more than 20 meters length and water speeds of 3-4 meters a modest heat flux of about 0.1 ... 0.5 W/cm²/°C can be utilized.

For more compact coil designs edge cooling is preferred, where the heat flux of 900 watts/cm² has been achieved.²⁰ Conductor discs with axial or radial cooling holes are not used in high-energy magnets. For coils with uniform current distribution, using rectangular hollow conductors, the power density in the coil may be calculated from

$$w_v = \frac{P}{2\pi a_1^3 (\alpha^2 - 1) \beta \lambda_1 \lambda_c} \quad (62)$$

where λ_1 and λ_c are the insulation and the conductor space factors, respectively. Using

$$\lambda_c = \frac{\pi d_h^2}{4\Delta^2}$$

the relation between w_v and the power per unit cooling area w_s is given by

$$\frac{w_v}{w_s} = \frac{\lambda_c}{1 - \lambda_c} \cdot \frac{4}{d_h} \quad (63)$$

with d_h as the hydraulic diameter.

Combining Eqs. (62) and (63) we get for the heat flux

$$w_s = \frac{d_h}{8\pi a_1^3 (\alpha^2 - 1) \beta \cdot \lambda_1} \cdot \frac{1 - \lambda_c}{\lambda_c^2}$$

Figure 16 illustrates the ratio $\frac{w_v}{w_s}$ versus $(4\Delta^2/\pi d^2 - 1)$ and the copper space factor. From experience, the choice of w_v/w_s and λ_c are simple, which gives d_h as a first approximation.

The number of cooling holes per unit cross section perpendicular to the flow direction is obtained from:

$$m = \frac{4}{\pi} \frac{w_v}{c\Delta\theta_b} \cdot \lambda_1 \cdot \lambda_c \cdot \left(\frac{s \cdot f}{\Delta p \cdot g}\right)^{\frac{1}{2}} \cdot \left(\frac{\rho^{3/2}}{d^{5/2}}\right) [\text{cm}^{-2}] \quad (64)$$

For a given pressure drop, the maximum current density may be calculated from

$$s^2 = \frac{c \cdot \Delta \rho}{\rho} \cdot \left(\frac{\Delta p \cdot g}{s \cdot f}\right)^{\frac{1}{2}} \cdot \left(\frac{d^{1/2}}{\rho^{3/2}}\right) \cdot \frac{\lambda_c}{1 - \lambda_c} \quad (65)$$

$$s^2 = \frac{c \cdot \Delta \theta}{4\rho} \cdot \left(\frac{\Delta p \cdot g}{s \cdot f}\right)^{\frac{1}{2}} \cdot \left(\frac{d^{3/2}}{\rho^{3/2}}\right) \cdot \frac{w_v}{w_s} \quad (66)$$

Stresses on the conductors due to magnetic and current forces and due to different thermal expansions between adjacent turns may be mentioned. However, detailed calculations reported by different authors for iron core magnets with up to 30-kG fields in the bore show that in most cases the tensile strength in the conductor does not exceed 100 kg·cm⁻², which is still safe for half-hard copper.²¹ However, winding half-hard copper conductors into a coil may show undesired distortions of the copper cross section and insulation damage.

A. Coil Insulation

Coil insulation can be regarded as the most delicate and sensitive part of the whole magnet. A sound conductor insulation guarantees the lifetime of the magnet. The insulation is subject to electrical, thermal, and mechanical stresses and ironization effect due to irradiation. In many cases, due to water condensation on coil surfaces, close to the water inlet manifolds, or leaks through joints, the insulation absorbs water and the insulation resistance and the dielectric strength are reduced considerably.²²

The aim of suitable coil insulation is to provide a reliable product that will perform its intended functions within the environmental conditions in which the magnet must operate. With the advancement of technology in high-energy accelerators, the demands on insulation have been increasing constantly. From simple cotton shellac insulation in the early magnets, modern accelerator magnets use high tensile strength, glass fiber reinforced thermosettings with additional mica and inorganic fillers.

If only high mechanical strength and moderate electrical stress in dry areas is required, glass fiber and high flexural strength epoxies may be sufficient. When magnets are subject to moisture and water vapor, protective coatings, or epoxy-impregnated polyester-web and mica may be used additionally in the ground insulation.

In a high irradiation environment ($> 10^{11}$ rads), high purity inorganic fillers are added to a suitable thermoset.²³ Highly filled epoxies show more affinity toward moisture absorption and their protection is more important. The water absorption

is enhanced when the ionization due to irradiation is continuous. Filled epoxies lose mechanical strength, but the right balance between radiation resistance and loss in mechanical and electrical strength and the addition of suitable wetting agents has to be studied carefully for each individual case. Needless to say, the manufacturing problems with these new filled thermosets are increased many-fold, compared to pure epoxy impregnants, and require new and better manufacturing techniques and studies of pot life, viscosity, wetting characteristics of the thermoset.

B. Magnet Core and Choice of Steel

In the design of high-energy magnets there is a distinct difference in the choice of steel for the ac accelerator magnets and the magnets for dc operation, such as beam transport and experimental magnets. Since several magnets may be powered by one power supply, it is required that the fields in the gap of each individual magnet should be within 10^{-2} to 10^{-3} of each other. Variations of the iron properties within a core or from different heats are required to be a minimum.

The ac magnets require low remanence fields and low coercive force in order to eliminate, if possible, the use of degaussing coils. It is also required that μ_r should be high at low flux densities.

In ac magnets, due to the effect of eddy current and hysteresis losses, the choice of 1-3% silicon steel is preferred^{24,25} over low carbon steels.

In alternating-gradient magnets with variable gaps the variation of permeability does influence the field in the gap. At high fields with permeability values of less than 100, the field gradient may be reduced by several percent. At low fields of less than 10^3 gauss the relative permeability may vary up to 28%, which influences the field in the midplane by about 1.5%.

Local heating in the core and nonuniform pressing of the core stack has undesirable effects on the permeability and the field distribution in the gap. In order to avoid local heating in bolts, and additional losses due to bolt holes, the 0.1^o SLAC deflection magnet core has omitted all bolts. The core was pressed by an hydraulic press, welded at the external surfaces, and impregnated with epoxy.⁶ The welding was performed such that iron crystal distortion and sheet undulation, which leads to nonuniform pressing in local spots and may ruin the properties of the iron,²⁶ were eliminated. Needless to say, undulation and nonuniform pressing also influence the mechanical tolerances of the gap.

Grain-oriented sheets, which have excellent magnetic and mechanical properties, can not be used due to the two-dimensional sheet structure. If the grain and flux directions are not parallel, the flux density in iron at a constant exciting magnetization force can change by more than 15% as a function of the deviation angle between flux and the rolling direction.²⁷

Hot rolled and cold reduced sheets with low loss factors and coercive force less than one are available commercially and have been used in accelerator magnets.¹⁰

Magnetization and permeability curves for different sheets manufactured from different ingots are given in Fig. 13. The curves are measurements of 10 samples and show the variation of relative permeability of different samples at 1 oersted to be about 28% and at 3.12 oersted about 20%.

The coercive force, which varied for the different samples measured, is

$$1.602 + 0.763$$

$$- 0.577$$

In order to reduce the coercive force, many laboratories specify the annealing of sheets in an N_2 atmosphere even if hot rolled sheets are used, which can result in a reduction of coercive force by more than 50%.

In high frequency magnets high flux density cores operating at 60 cps or higher (360 cps at SLAC) are subject to compression and relaxing forces, which are variable over the core due to different core saturations. The hammering effect accelerates the core fatigue, and the magnetic properties may deteriorate within the lifetime of the magnet. The compromise in choosing low flux density in iron to improve reliability, the magnet price, and space limitation is again a problem each laboratory has to cope with.

In dc magnet cores the effect of small amounts of impurities in the form of nonferro-magnetic materials, gas channels, voids, cracks, etc., has been investigated by various authors.²⁸ Forged steel is usually preferred over cast steel, even if the price of forgings is slightly higher. In poles, due to the high homogeneity requirements in the gap, exceedingly pure steels are preferred. In yokes, a compromise in choice of less expensive steels is permissible. The alloying elements in the steel form compounds, which are deposited in steel crystal boundaries or as grains in pure iron. Hedin⁵ derives relations for macroscopic flux density and field strength in a structure with nonmagnetic compounds occupying p parts per weight of the pure iron. His conclusions, which are in agreement with measurements carried out by CERN and BNL, show that for a total amount of 2 parts per weight impurities, carbon has by far the strongest influence. Next important elements are Al, Mo, S and P, which have a detrimental effect on magnetic properties. The third group of elements are Mn, Ni, Cr, Cu and Si.

However, many of these elements are required for forging or casting reasons; Al and Si, for example, are used to reduce gas bubbles in the cast. Impurities have a tendency to agglomerate in the top part of the ingot. SLAC specified that about 1/3 of the value should be cut off and removed, which results in a fairly pure steel structure. Depending on the source of the ore, wide tolerances on the impurity compositions may be allowed, but the total amount of impurities must be limited.

SLAC specifies for dc magnet steels:

C	max. 0.1...0.12	p.p.w.
Total Al + Mo + S + P	max. 0.1	p.p.w.
Total Mn + Ni + Cr + Cu + Si	max. 0.7	p.p.w.

Lowering the carbon content leads to a very soft steel structure which is undesirable in core manufacturing to attain close gap tolerances and is expensive.

VI. Conclusion

The design of electromagnets for high-energy physics applications has undergone considerable improvement in recent years. However, due to many conflicting requirements in every magnet, the proper evaluation and balance of the different parameters is the paramount problem of the magnet designer. With the growth of the high-energy accelerators the need for large magnets is still growing. Bubble chamber and spark chamber magnets with $2a_1 = 2 - 5$ meters bore are presently under construction. Large bore magnets ($2a_1 = 1 - 2$ meter) with fields more than 100 kG are under investigation. However, the power consumption of such dc magnets (60-200 MW) with water cooling seems economically unsound, and possibilities for pulsed and superconducting magnets seem feasible. Iron-bound high field magnets are still attractive. They contribute up to 16% to the fields generated by the coil ampere-turns in high field magnets. In many areas the classical coil design with hollow conductors may be abundant for more efficient magnets with higher values of heat flux, w_s . To make better use of the iron in combination with coils, a thorough understanding of the flux pattern in iron is necessary. A program calculating two-dimensional potential problems has been developed; however, three-dimensional potential problems are still in the investigation stage. Matching field shapes to particle optics is also one of the important problems and deserves more thorough study.

Acknowledgement

The author is indebted to Dr. Karl Brown of the Stanford Linear Accelerator Center for many fruitful discussions and helpful suggestions, and to Dale Borglum of Stanford University, Lee Anderson of Oregon State University, who joined the Magnet Research Group a short time ago and Ed Burfine SLAC for their active work in the Nutcracker program.

References

1. K. L. Brown, "Some useful theorems based on a general first-order theory of image formation," SLAC Internal Report, Stanford Linear Accelerator Center, Stanford, California (1964).
2. B. deRaad, "Methods to calculate beam transport systems," CERN Report, CERN, Geneva, Switzerland.
3. R. H. Helm, "Discussion of focusing requirements for the Stanford two-mile accelerator," SLAC Report No. 2, Stanford Linear Accelerator Center, Stanford, California (1962).
4. H. A. Enge, Rev. Sci. Instr. 2 35, 278 (1964).
5. B. Hedin, "A bending magnet with non-saturating shimming," SLAC Report No. 19, Stanford Linear Accelerator Center, Stanford, California (1963).
6. H. Brechna, "A pulsed bending magnet for the beam switchyard area of the Stanford two-mile linear electron accelerator," SLAC Report No. 28, Stanford Linear Accelerator Center, Stanford California (1964).
7. M. S. Livingston and J. P. Blewett, Particle Accelerators (McGraw Hill, New York, 1962).
8. J. H. Dorst, "A computer program for magnet design," LRL Report UCID-10022, (Lawrence Radiation Laboratory, Berkeley, California 1954).
9. A. M. Winslow, "Numerical calculation of static magnetic fields in an irregular triangle mesh," LRL Report UCRL-7784, Lawrence Radiation Laboratory, Berkeley, California (1964).
10. W. Hardt, "Ueber die Gestaltung des DESY Magneten," DESY Report A.1.5, DESY, Hamburg, Germany, (1959).
11. "The design of quadrupole lenses for the proton synchrotron," CERN PS/MM 31, CERN, Geneva, Switzerland (1957).
12. H. Hultschig, "Zur Entwicklung der Quadrupollinsen," DESY Notiz A 2.76, DESY, Hamburg, Germany (1961).
13. H. Kumagai, Nucl. Inst. and Methods 6, 213-216 (1960).
14. M. H. Blewett, "An analytical method for designing multiple magnets," NBL Internal Report (Oct. 1957).
15. F. Bitter, Rev. Sci. Instr. 7, 482-488 (1936).
16. F. Gaume, "Coils without iron for the production of very intense continuous magnetic fields. Calculation and realization," CNRS No. 43, June 1958 (Transl. H. H. Kolm, Lincoln Laboratory Report M81-12).
17. G. V. Brown, et al. "Axial and radial magnetic fields of thick, finite-length solenoids," TN R-170 Lewis Research Center (1963).
18. W.J.C. Grant and M.W.P. Strandberg, Rev. Sci. Instr. 36, (1965).
19. F. Bitter, Rev. Sci. Instr. 7, 479-481 (1936).
20. H. Brechna and D. B. Montgomery, "A high performance dc magnet utilizing axial cooled discs," Report NML-62-I, Massachusetts Institute of Technology, Cambridge, Massachusetts (1962).
21. F. Bitter, Rev. Sci. Instr. 33, 342-349 (1962).
22. H. Brechna, "Magnetic focusing lenses," Bulletin Oerlikon No. 346-347, Oerlikon, Switzerland, (Dec. 1961); pp. 79-105.

23. H. Brechna, "Effect of nuclear radiation on organic materials, specifically magnet insulation in high energy accelerators," SLAC Report No. 40, Stanford Linear Accelerator Center, Stanford, California (1965).
24. "Etude des proprietes magnetiques des toles des aimants du synchrotron a protons," CERN-PS-MM 18, CERN, Geneva, Switzerland.
25. M. H. Blawett, "Magnet design in high energy accelerators," IEEE Trans on Nuclear Scienc NS-12 317-326 (1965).
26. H. Brechna, "Some aspects of modern transformer core design," Recent Developments in Transformer Design, Oerlikon, Switzerland (1960); pp. 4-12.
27. H. Brechna, "New design trends in the construction of transformer cores," Recent Developments in Transformer Design, Oerlikon, Switzerland (1960); pp. 14-22.
28. R. M. Bozorth, Ferromagnetism (D. van Nostrand, New York, 1951).
29. H. Brechna and W. Haldeman, "Physical properties of filament-wound glass epoxy structures as applied to possible use in liquid hydrogen bubble chambers," presented at the 1965 Cryogenic Engineering Conference, Rice University, Houston, Texas, August 23-25, 1965.

FIGURES

ELECTROMAGNETS FOR HIGH ENERGY ACCELERATORS

Fig. 1 Phase Ellipse

Fig. 2 Path and Trajectories of a Charged Particle in a
Three Dimensional Magnetic Field

S = Normal Path

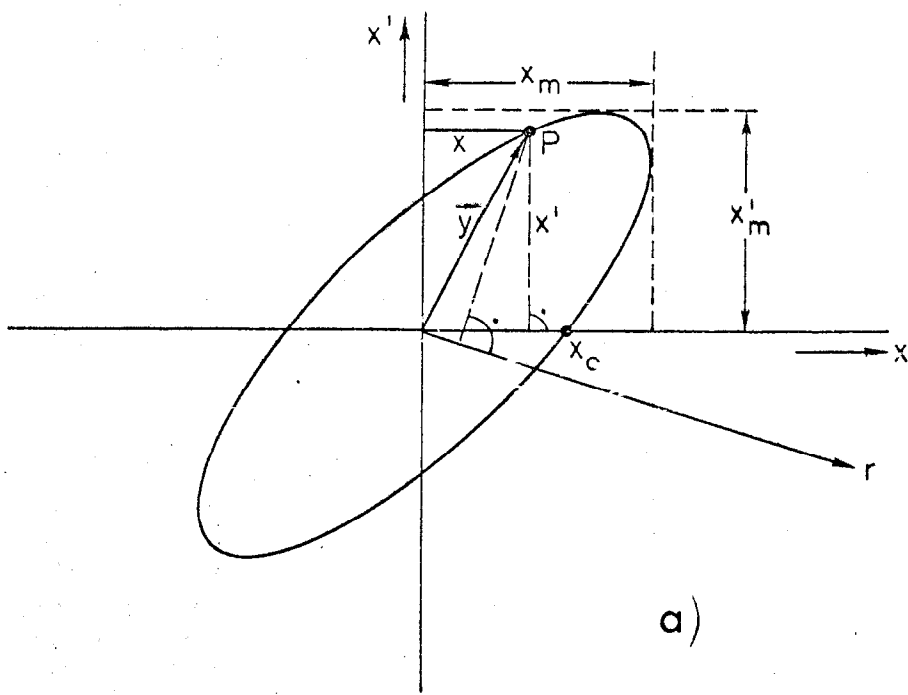
S' = Trajectory in the x-z plane

S = Central Trajectory

Fig. 3 Pole Shaping and Field Distribution.

- (1) Measured field distribution.
- (2) Midplane field distribution neglecting saturation.
- (3) Midplane field distribution according to pole contour b.
- (4) Flux density at pole contour b.
- (5) Field distribution according to pole contour c.
- (6) Flux density at pole contour c.
- (7) Midplane flux distribution according to pole contour d.
- (8) Flux density at pole contour d.
- (9) Midplane flux distribution according to pole contour e.

- Fig. 4 Polecorner Shimming
- Fig. 5 Simplified polecorner Shimming
- Fig. 6 Pole Contour Shimming for AGS Magnets
- Fig. 7 Model to Calculate Saturation Effect
- Fig. 8 Pole End Shaping
- Fig. 9 Superposition of Linear and Quadrupole Fields
- Fig. 10 Field Calculation of a Bubble Chamber Magnet Assuming
Circular Symmetry and Uniform Iron Magnetization
- | | |
|-------------------|-------------------|
| 1 and 8: 20.7 kG | 2 and 7: 21.19 kG |
| 3 and 6: 21.13 kG | 4 and 5: 21.0 kG |
- Fig. 11 \tilde{F} factors for Solenoids with Uniform Current Distribution
- Fig. 12 Magnetic Dipoles
- Fig. 13 Measured and Calculated Magnetization Curves
1. Silicon Iron
 2. 0.1% Low Carbon Steel
 3. 0.12% Low Carbon Steel
 4. Calculated Magnetization Curve
- Fig. 14 Bubble Chamber Magnet Field Calculation for two-dimensional
Geometry Using Variable μ_r and A
- Fig. 15 Model for Three Dimensional Field Calculation
- Fig. 16



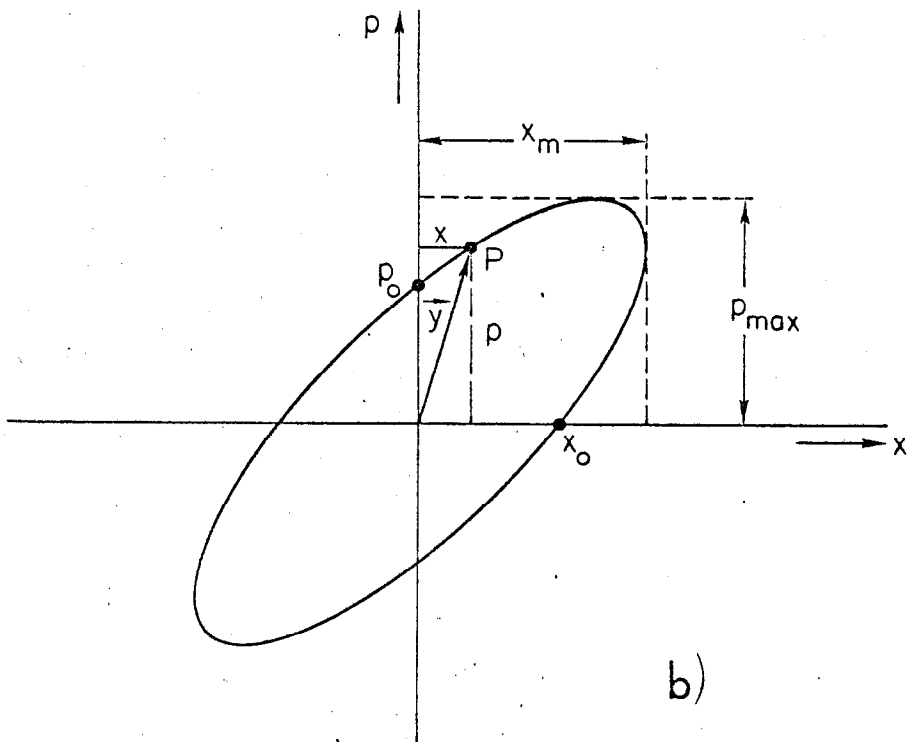
$$x'_m = C^{\frac{1}{2}}$$

$$x_m = F^{\frac{1}{2}}$$

$$\vec{y} = \langle x | x' \rangle$$

a)

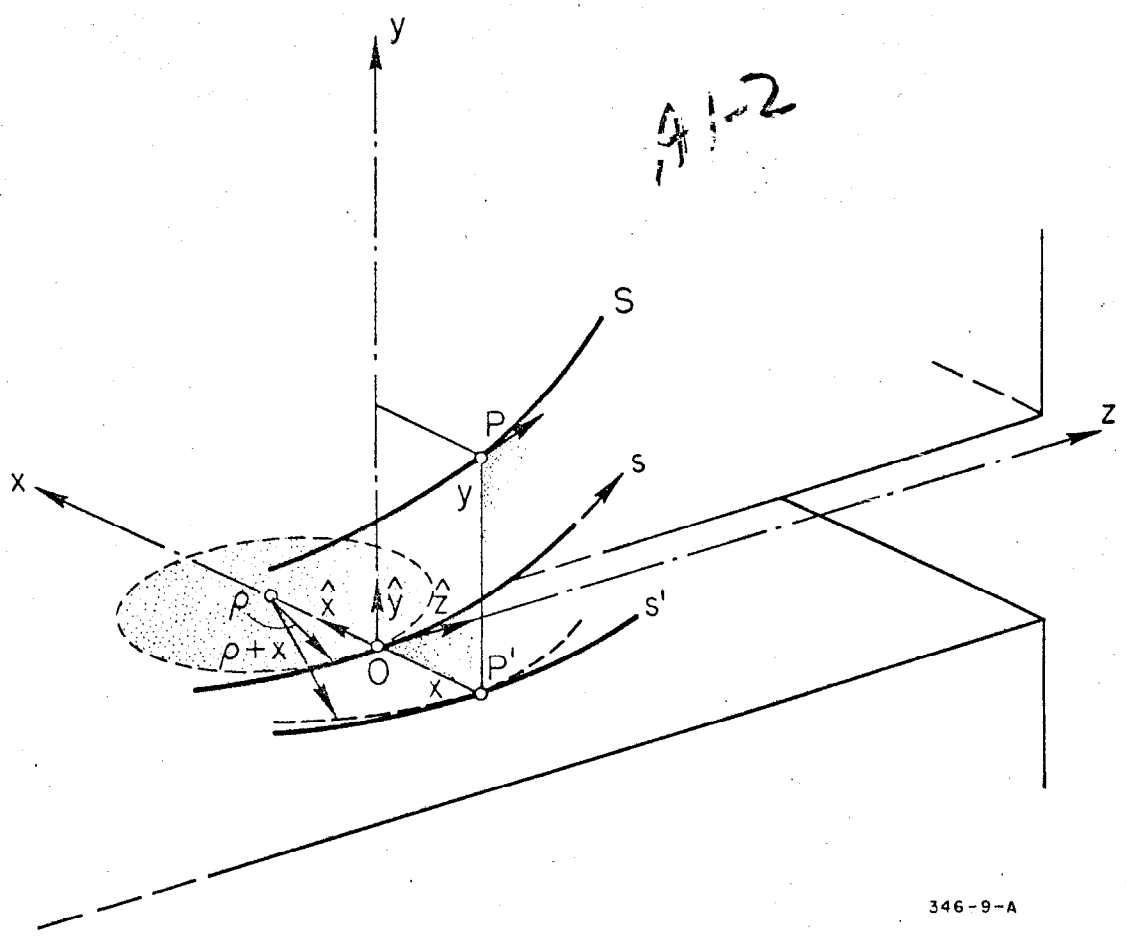
A1-1



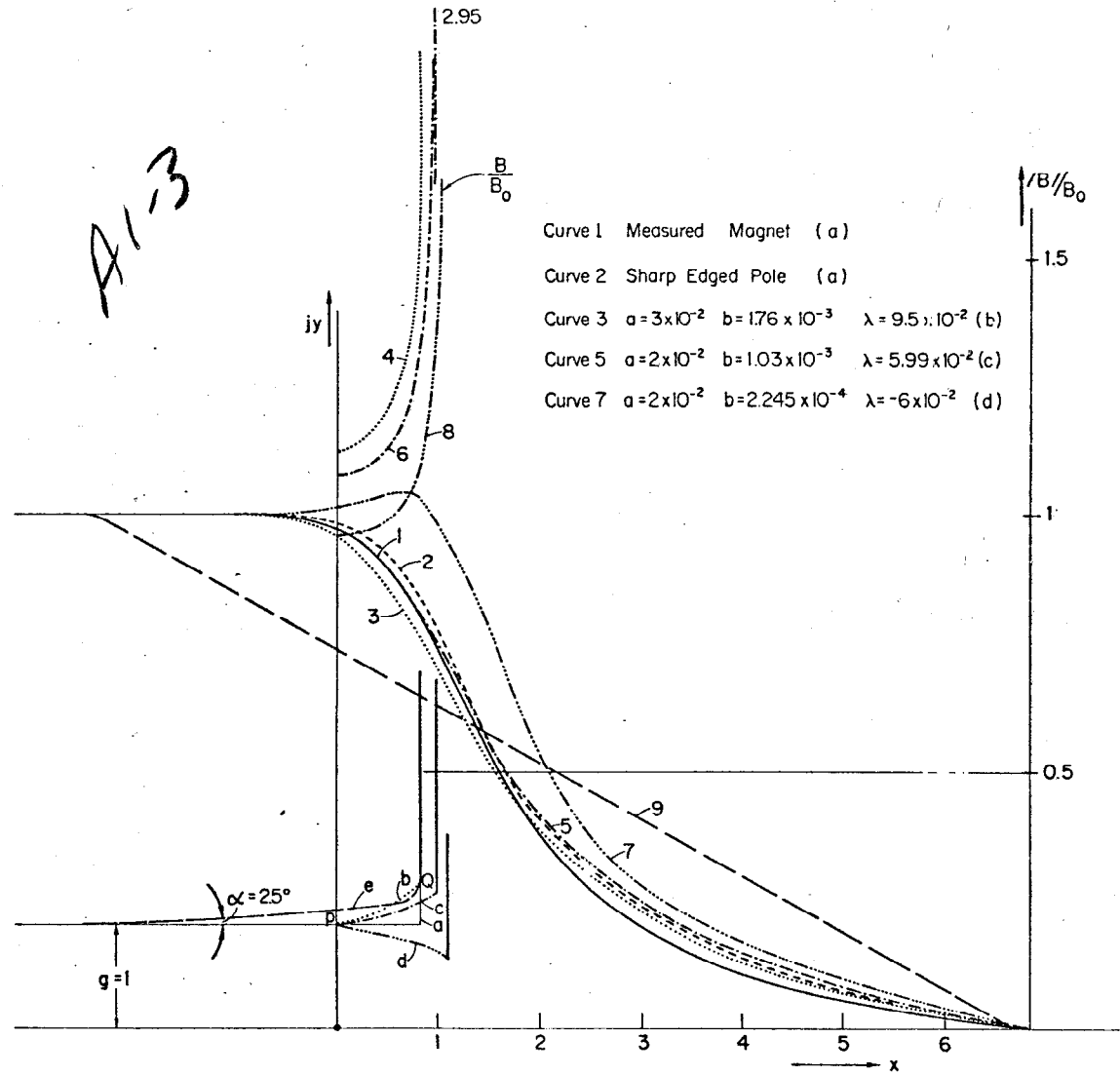
$$x_m = \frac{F}{CF - B^2}$$

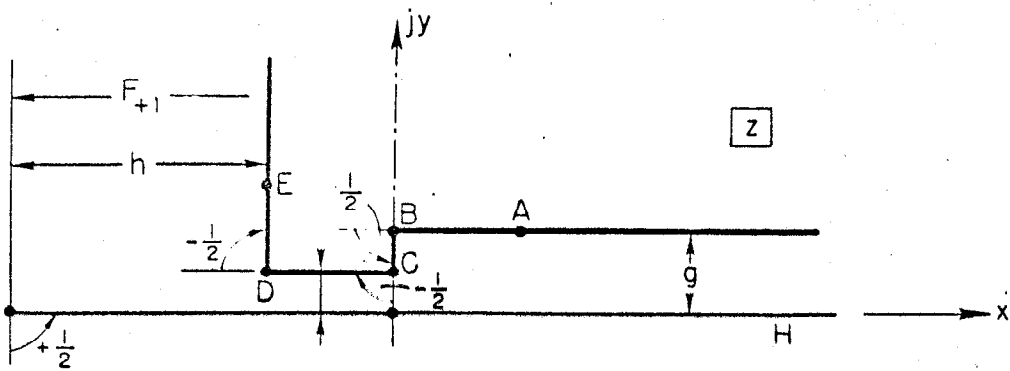
b)

A1-2

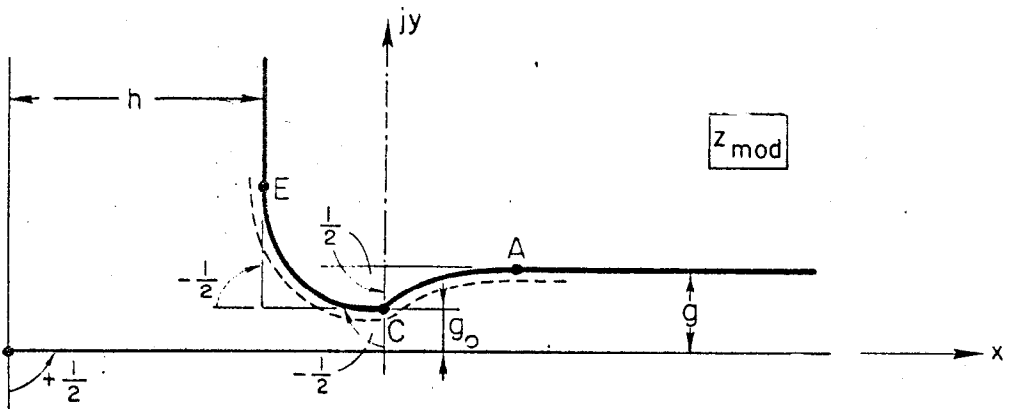


A1-3

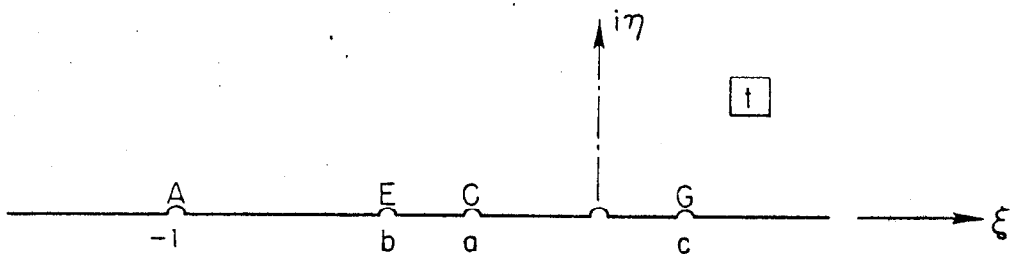




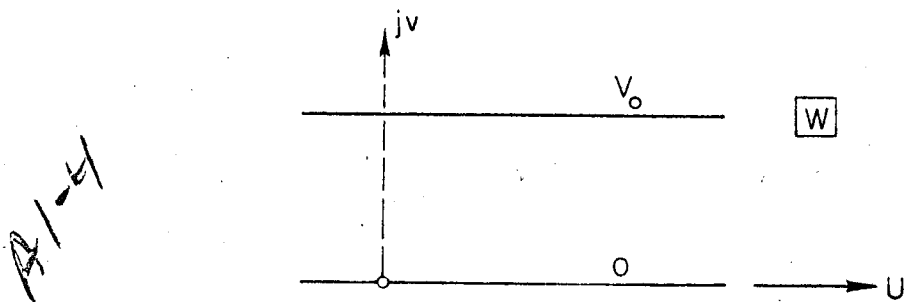
a)



b)



c)

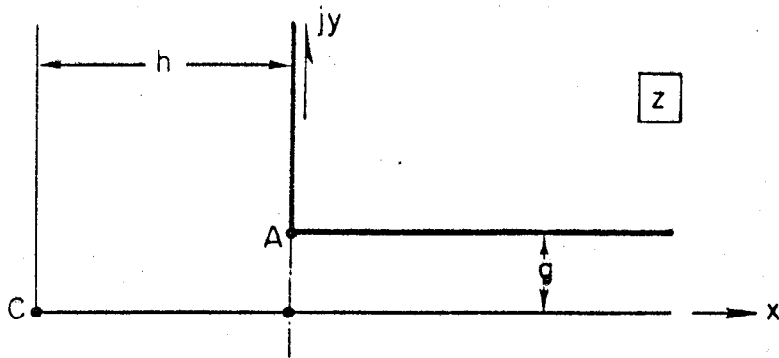


d)

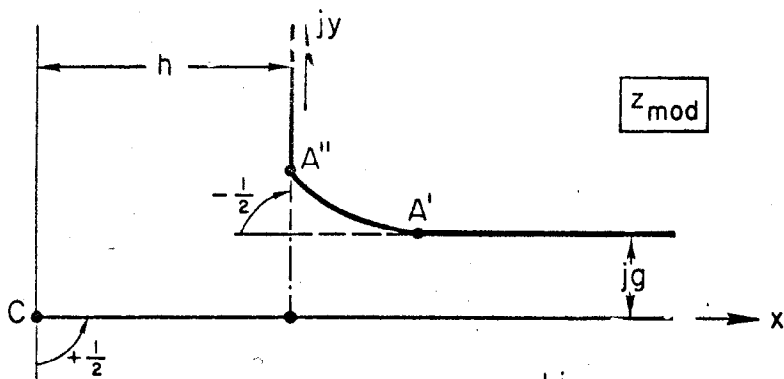
A1-4

$$z = \frac{g}{\pi} \int \frac{\left[\lambda_2 + (1 - \lambda_2) \left(\frac{t+b}{t+a} \right)^{\frac{1}{2}} \right] (t+a)^{\frac{1}{2}}}{\left[\lambda_1 \left(\frac{t+1}{t+a} \right)^{\frac{1}{2}} + 1 - \lambda_1 \right] (t-c)^{\frac{1}{2}}} dt + C$$

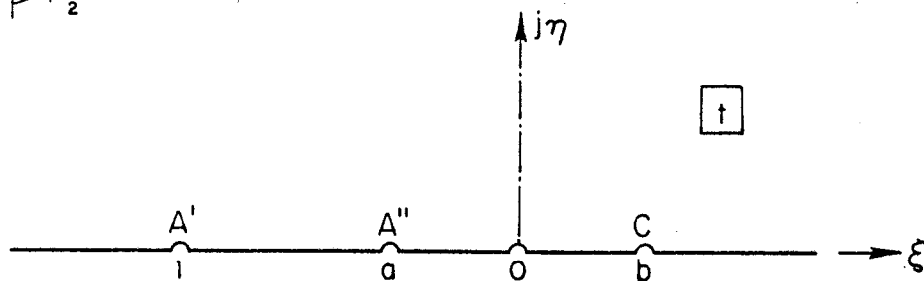
$$\frac{dW}{dz} = B_x + jB_y = \frac{V_0}{g} \cdot \frac{\left[\lambda_1 \left(\frac{t+1}{t+a} \right)^{\frac{1}{2}} + 1 - \lambda_1 \right] (t-c)^{\frac{1}{2}}}{\left[\lambda_2 + (1 - \lambda_2) \left(\frac{t+b}{t+a} \right)^{\frac{1}{2}} \right] (t+a)^{\frac{1}{2}}}$$



a)

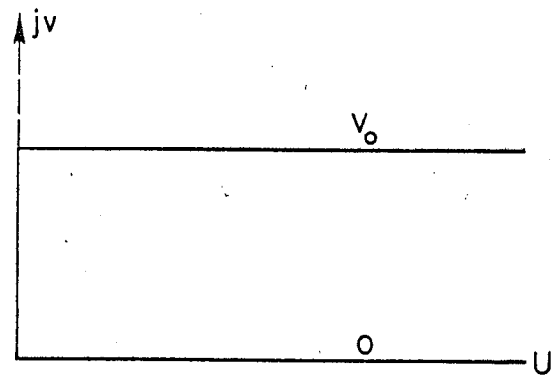


b)



c)

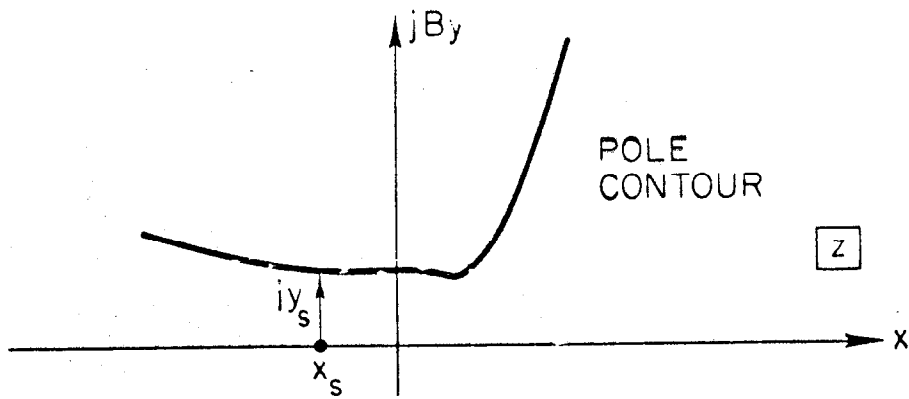
A/S



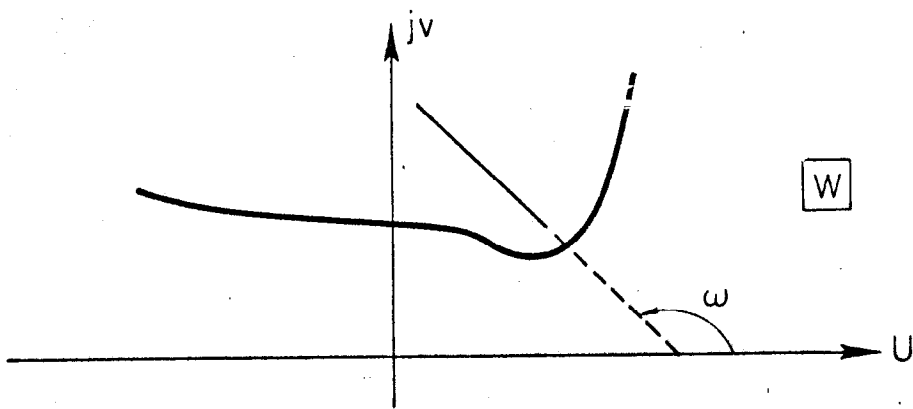
d)

$$z = \frac{g}{\pi} \int \frac{\lambda(t+1)^{\frac{1}{2}} + (1-\lambda)(t+a)^{\frac{1}{2}}}{t(t-b)^{\frac{1}{2}}} dt + C$$

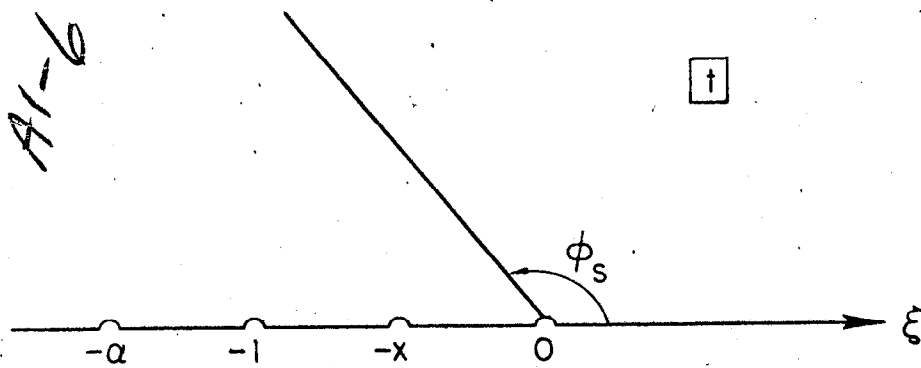
$$\frac{dW}{dz} = B_x + jB_y = \frac{V_0}{g} \cdot \frac{(t-b)^{\frac{1}{2}}}{\lambda(t+1)^{\frac{1}{2}} + (1-\lambda)(t+a)^{\frac{1}{2}}}$$



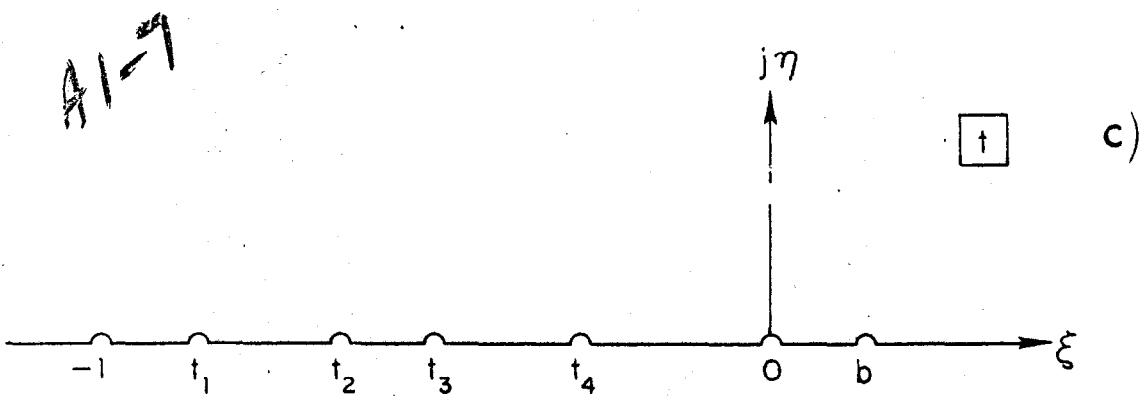
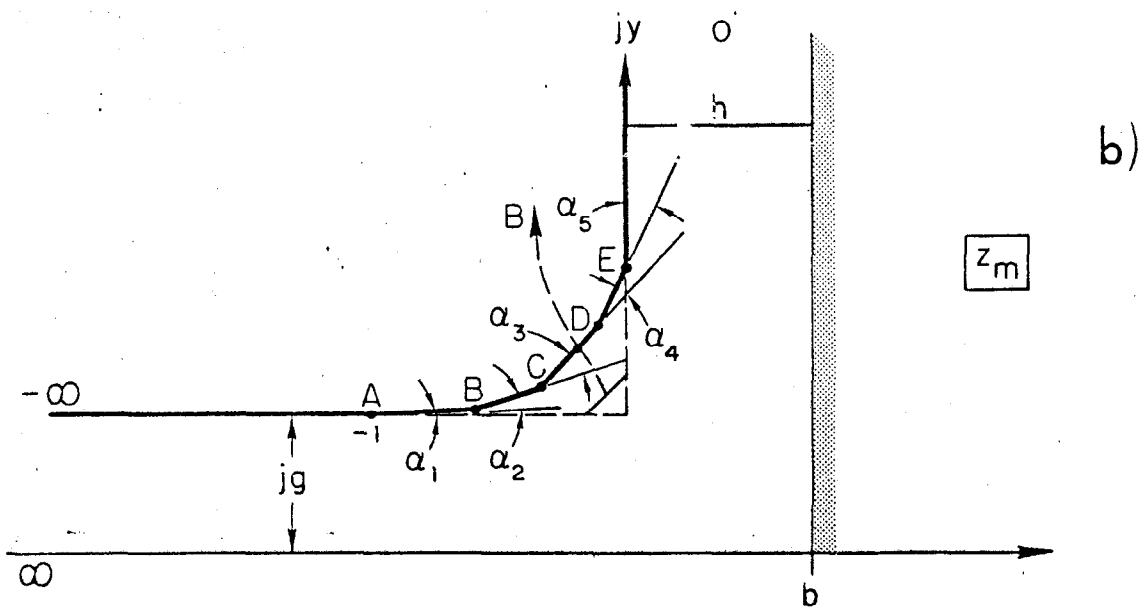
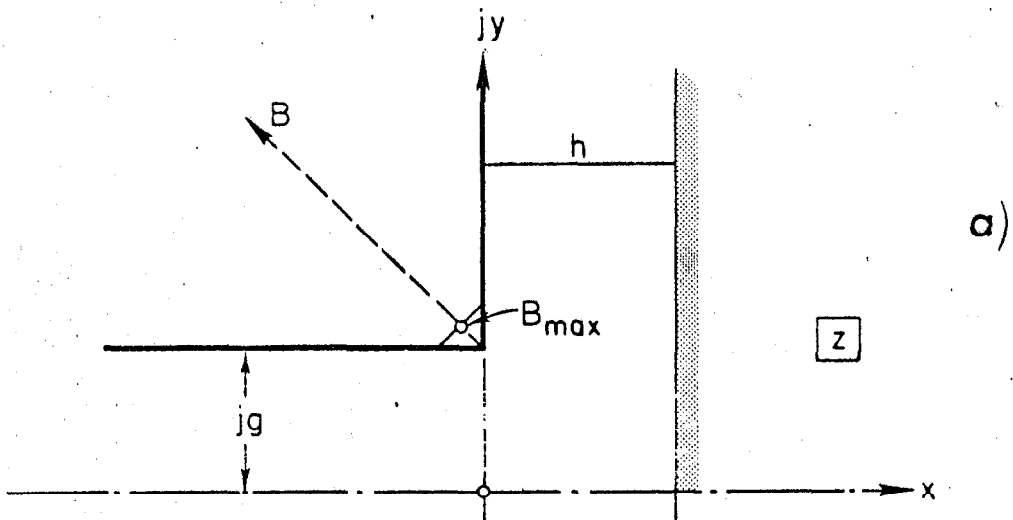
a)

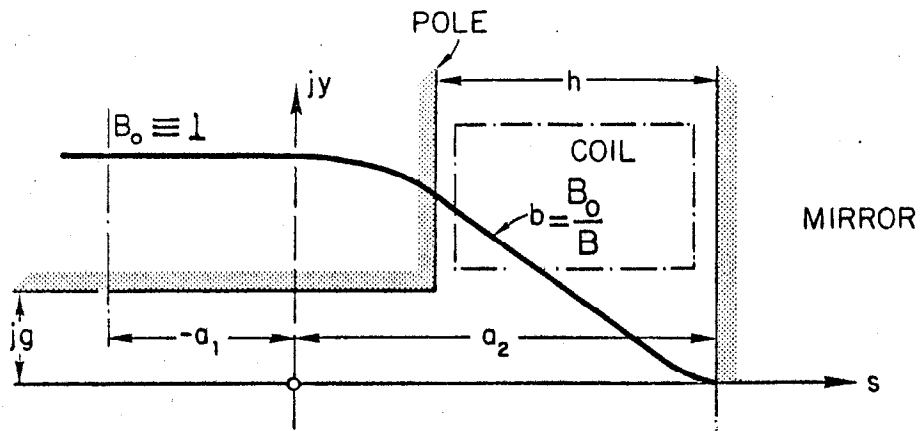


b)

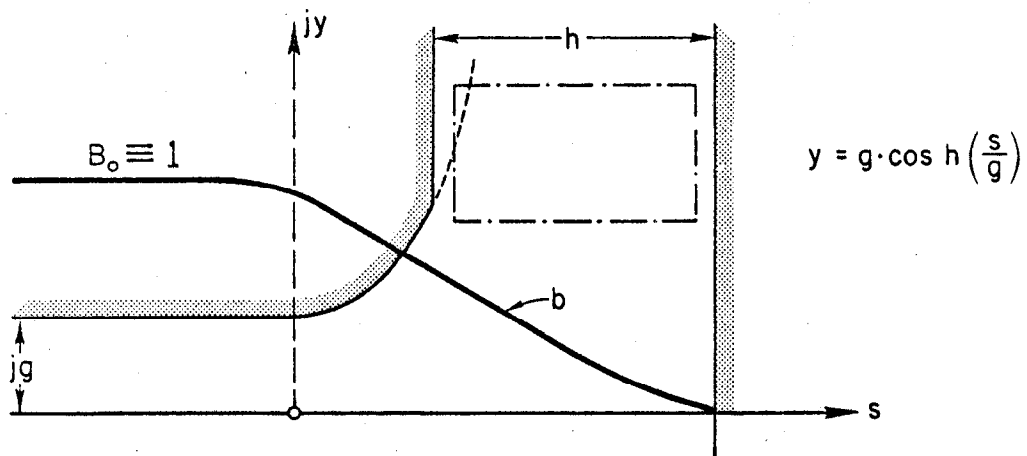


c)

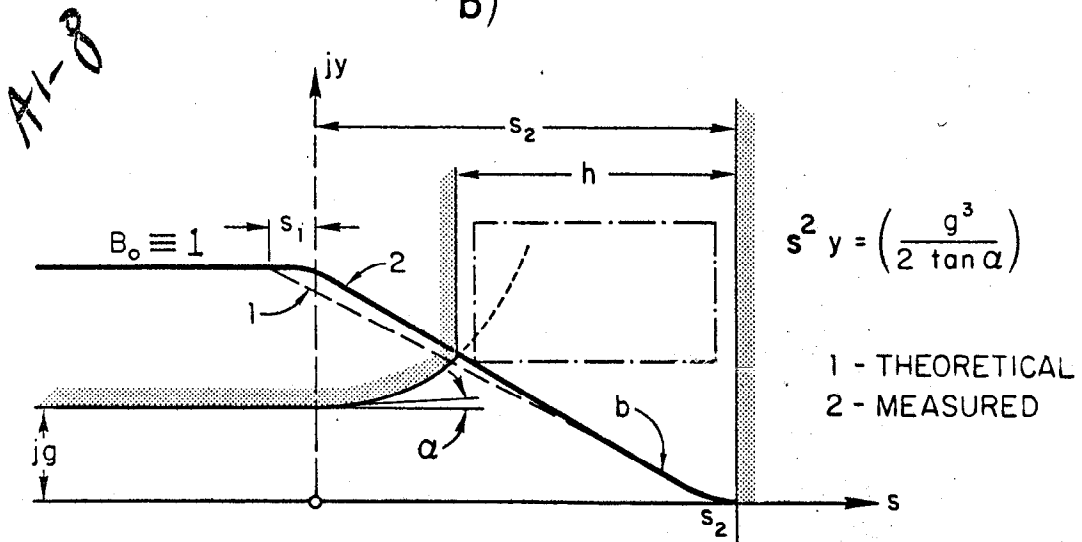




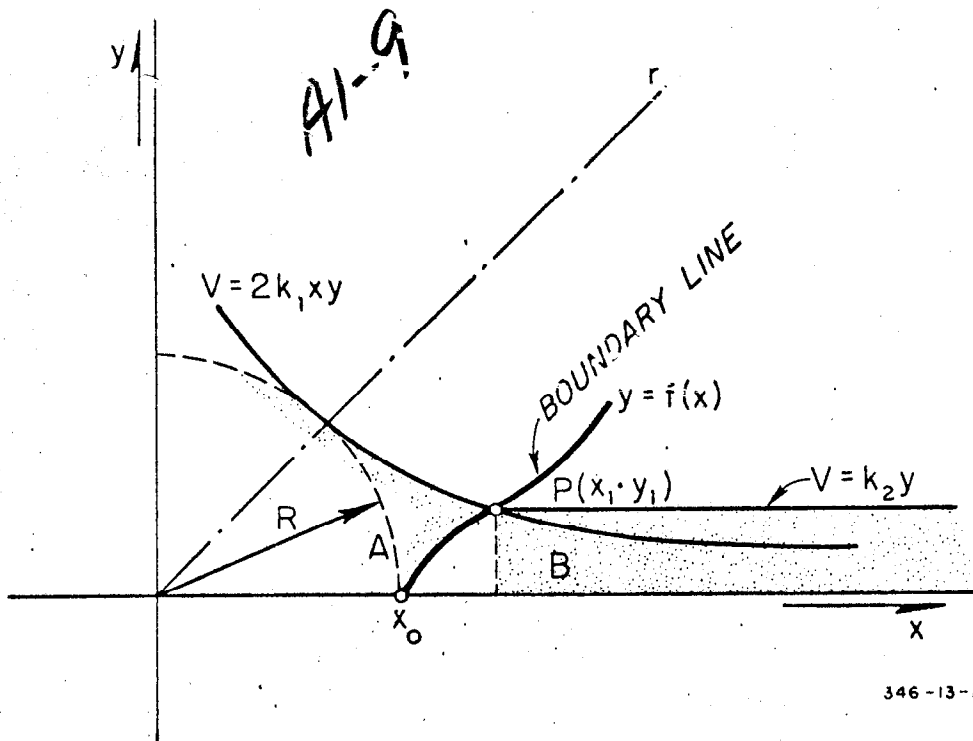
a)

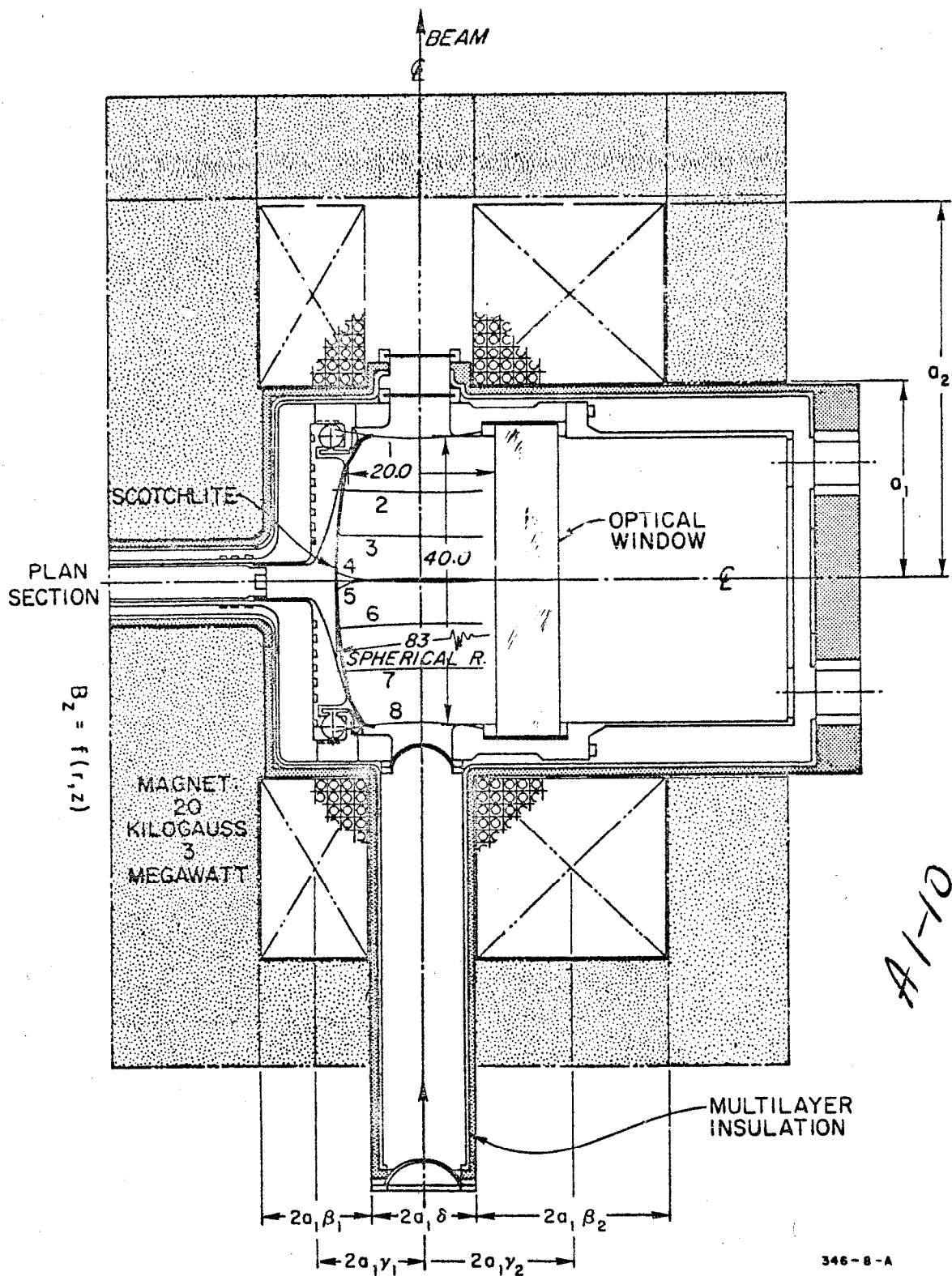


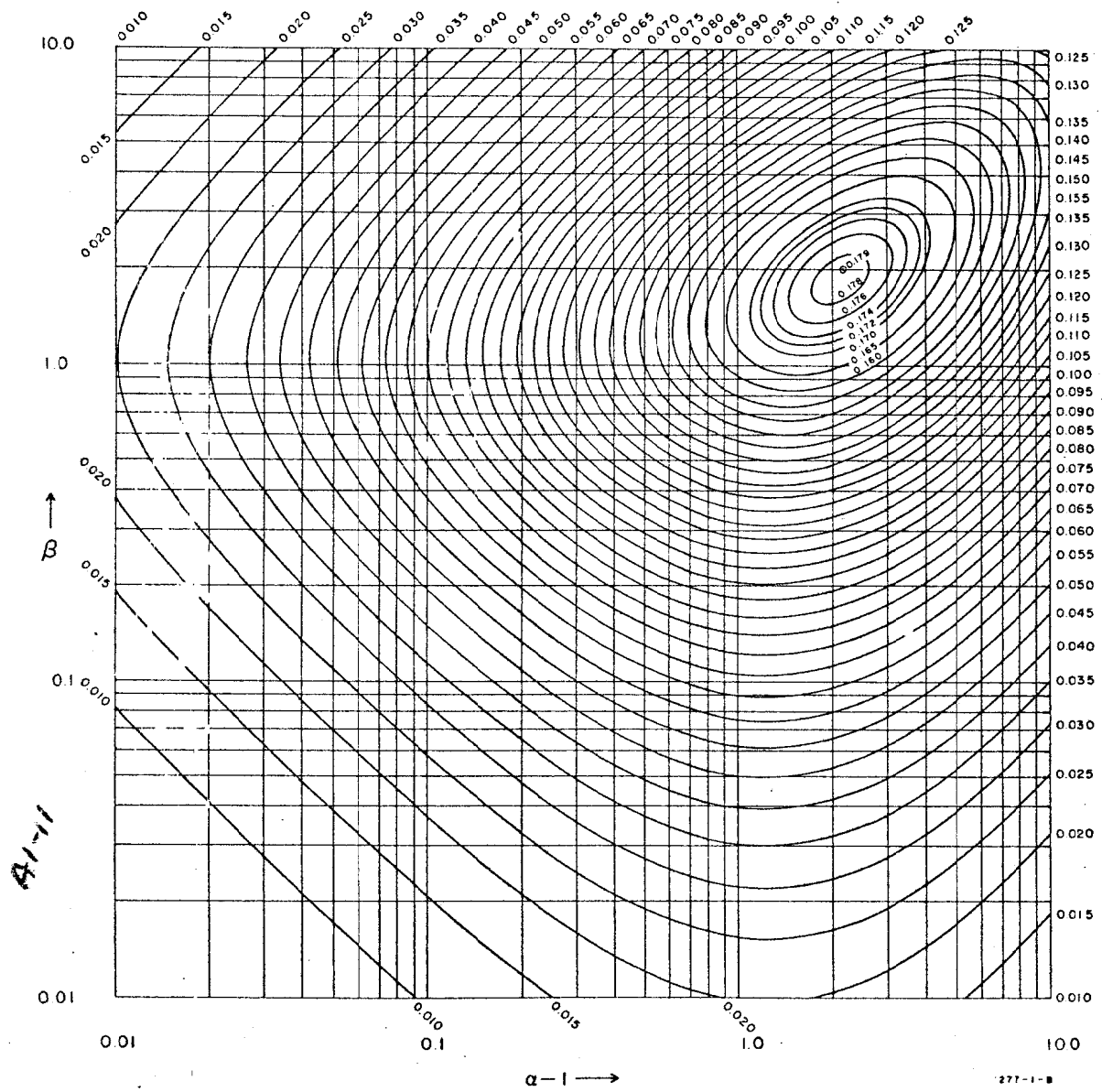
b)

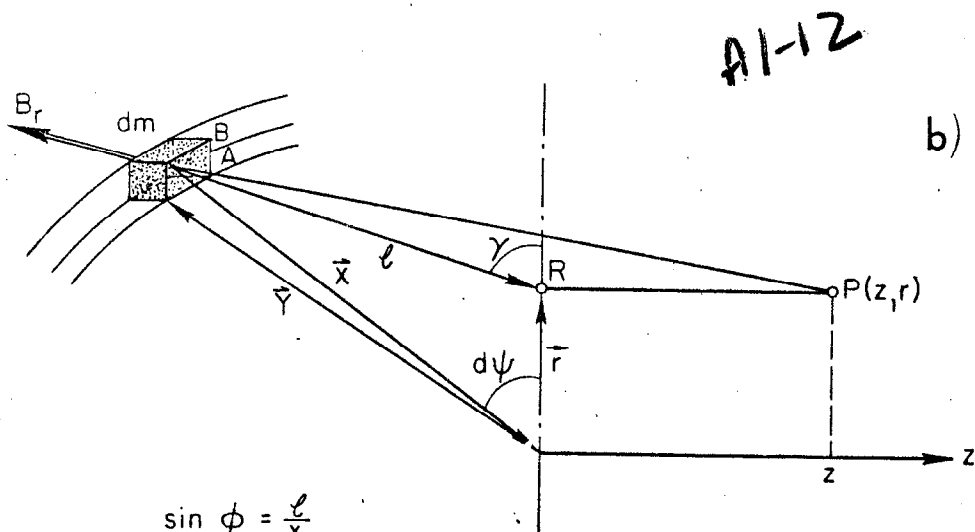
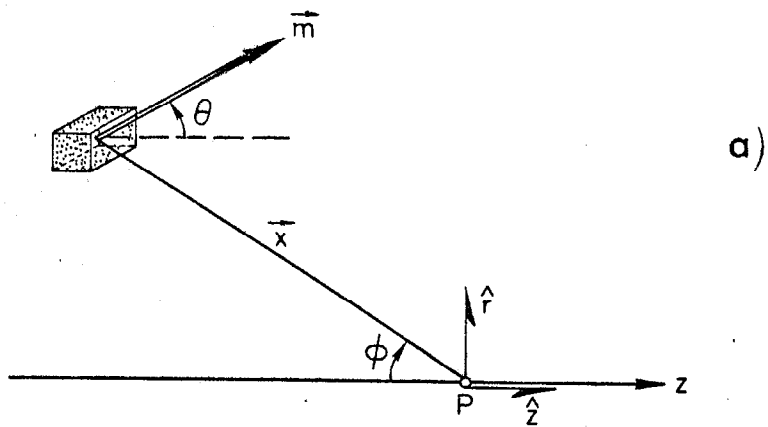


c)









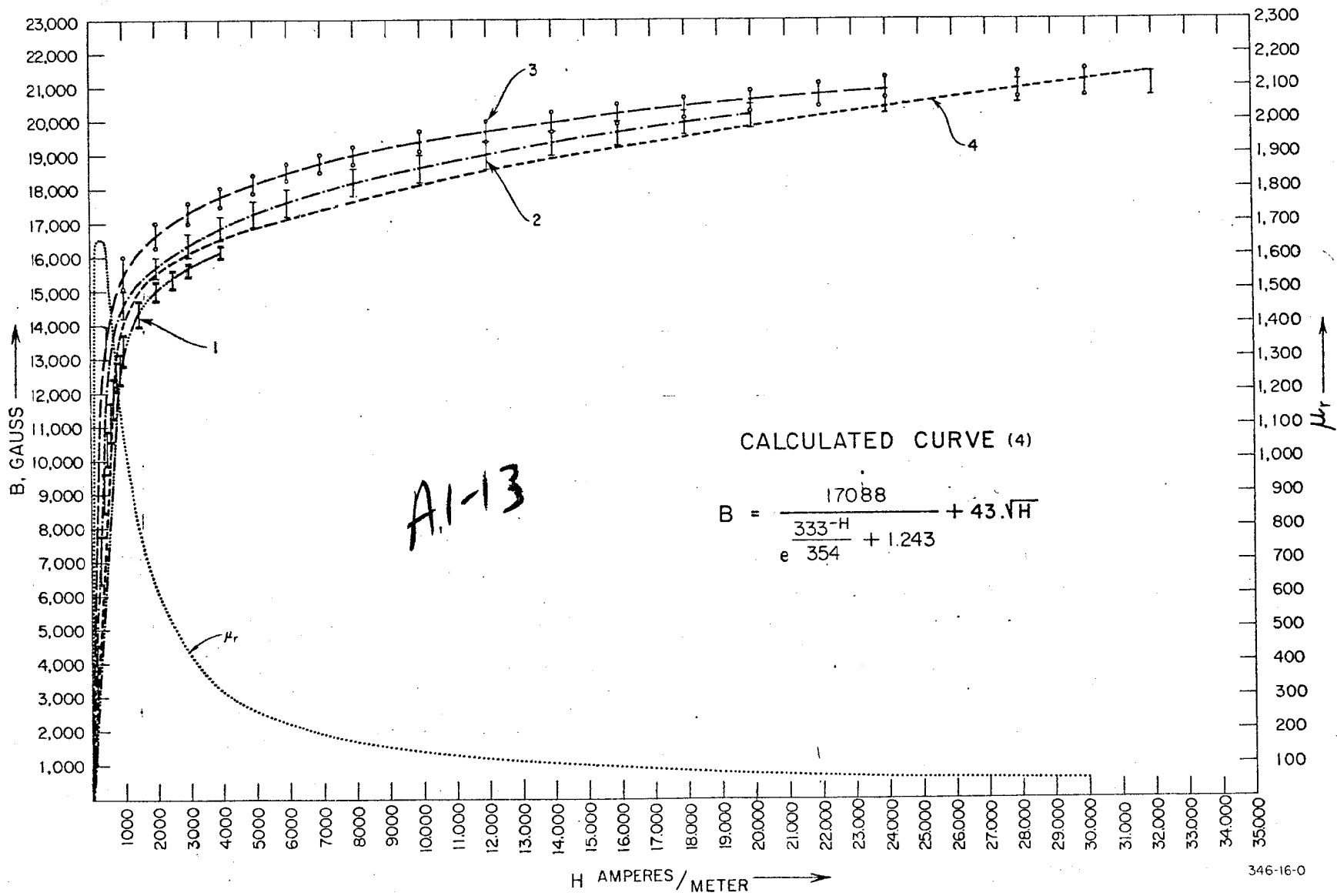
$$\sin \phi = \frac{l}{x}$$

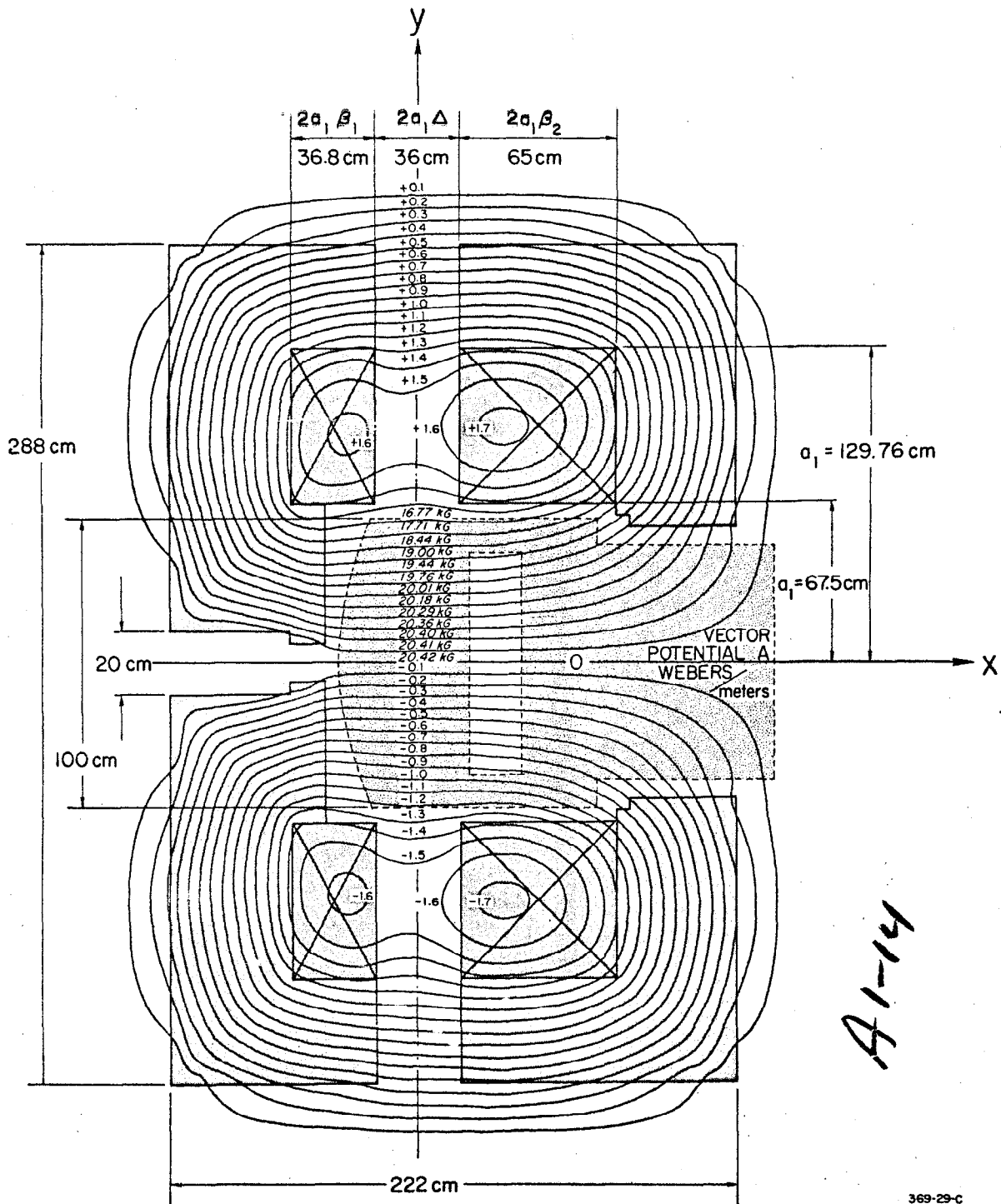
$$\cos \phi = \frac{z}{x}$$

$$\cos \gamma = \frac{Y \cos \phi - r}{l}$$

$$dm = A \cdot B \cdot Y d\phi \cdot M$$

= DIPOLE DIFFERENTIAL VOLUME





A1-14

